Journal of Asian Earth Sciences 115 (2016) 442–454

Contents lists available at ScienceDirect

Journal of Asian Earth Sciences

journal homepage: www.elsevier.com/locate/jseaes

Geochronology and geochemistry of the high Mg dioritic dikes in Eastern Tianshan, NW China: Geochemical features, petrogenesis and tectonic implications

Deng-Feng Li [a,b,c], Li Zhang [a,*], Hua-Yong Chen [a], Pete Hollings [c], Ming-Jian Cao [d], Jing Fang [a,b], Cheng-Ming Wang [a,b], Wan-Jian Lu [a,b]

[a] Key Laboratory of Mineralogy and Metallogeny, Chinese Academy of Sciences, Guangzhou 510640, China
[b] Graduate University of Chinese Academy of Sciences, Beijing 100049, China
[c] Department of Geology, Lakehead University, 955 Oliver Road, Thunder Bay, Ontario P7B 5E1, Canada
[d] Key Laboratory of Mineral Resources, Institute of Geology and Geophysics, Chinese Academy of Sciences, Beijing 100029, China

ARTICLE INFO

Article history:
Received 21 May 2015
Received in revised form 11 October 2015
Accepted 22 October 2015
Available online 23 October 2015

Keywords:
High Mg dioritic dikes
Mantle-derived magma
Eastern Tianshan
Central Asian Orogenic Belt

ABSTRACT

Zircon U–Pb ages of high Mg dioritic dikes in the Mesoproterozoic Kawabulake Group in the Eastern Tianshan area, NW China indicate that they were emplaced in the Early Carboniferous at 353–348 Ma. The dikes consist of medium-grained plagioclase and hornblende with minor clinopyroxene and trace quartz. They are characterized by intermediate SiO_2 (60–62 wt.%), low TiO_2 (0.63–0.71 wt.%), relatively high Al_2O_3 (15.1–15.8 wt.%) and MgO contents (3.45–4.15 wt.%) with Mg# generally higher than 56 (56–59). The geochemistry of the high Mg diorites suggest they were formed by similar magmatic processes to sanukitoid high Mg Andesites such as those of the Setouchi volcanic belt, Japan. Zircons from the high Mg dioritic dikes have $\varepsilon Hf(t)$ values of −6.8 to +14.5. The dominantly positive values suggest a juvenile source, whereas the small number of negative values suggests mature components were also incorporated into the source. Similarly, the positive $\varepsilon Nd(t)$ values (0 to +2.2) are interpreted to reflect a juvenile source whereas the negative values of (−5.2 to 0) suggest participation of old crustal rocks in the petrogenesis of the diorites. The variable $\varepsilon Hf(t)$ and $\varepsilon Nd(t)$ values suggest that the mature material was assimilated during magma ascent rather than in the mantle wedge which would result in more uniform values. Mass balance calculations suggest that the dioritic dikes were derived from sources composed of approximately 97% juvenile mantle-derived material and 3% sediment. Petrographic, elemental, and isotopic evidence suggest that the dioritic dikes were generated by partial melting of depleted mantle that migrated into the shallow crust where it assimilated older sedimentary rocks of the Mesoproterozoic Kawabulake Group.

© 2015 Published by Elsevier Ltd.

1. Introduction

The Central Asian Orogenic Belt (CAOB), also known as the Altaid orogenic collage (Sengör and Natal'In, 1996), the Central Asian Orogenic Super collage (Windley et al., 2007; Yakubchuk, 2004) and the great Central Asian Orogenic Belt (Jahn, 2004; Jahn et al., 2000a,b,c), extends from the Uralides in the west to the Pacific margin in the east, including orogenic areas in Russia (Altai-Sayan, Transbaikalia, Primorje), East Kazakhstan, Kyrgyzstan, Uzbekistan, China, and Mongolia (Fig. 1a; Safonova et al., 2011). The CAOB is one of the world's largest accretionary orogens and evolved over a period of some 750 million years from about 1000 to 250 Ma (Jahn, 2004; Jahn et al., 2000a,b,c).

The Chinese Eastern Tianshan is the easternmost segment of the Tianshan Mountain Range located in the middle of CAOB (Fig. 1a; Xiao et al., 2004). High Mg diorites have been recognized in the Junggar area (to the north of the Eastern Tianshan) and have been proposed to be high-Mg andesites (HMA) associated with ridge subduction (Tang et al., 2010a,b; 2012a,b,c; Yin et al., 2010). These dikes show close compositional similarities to HMA that have been proposed to form through partial melting of depleted mantle (Drummond et al., 1996; Yogodzinski et al., 1994). This paper reports major and trace element geochemistry, MC-LA-ICP-MS zircon U–Pb ages and Hf isotopes and whole rock Sr–Nd–Pb of

* Corresponding author at: Guangzhou Institute of Geochemistry, Chinese Academy of Sciences, P.O. Box 1131, Tianhe District, Guangzhou 510640, Guangdong, China.
E-mail address: lizhang@gig.ac.cn (L. Zhang).

http://dx.doi.org/10.1016/j.jseaes.2015.10.018
1367-9120/© 2015 Published by Elsevier Ltd.

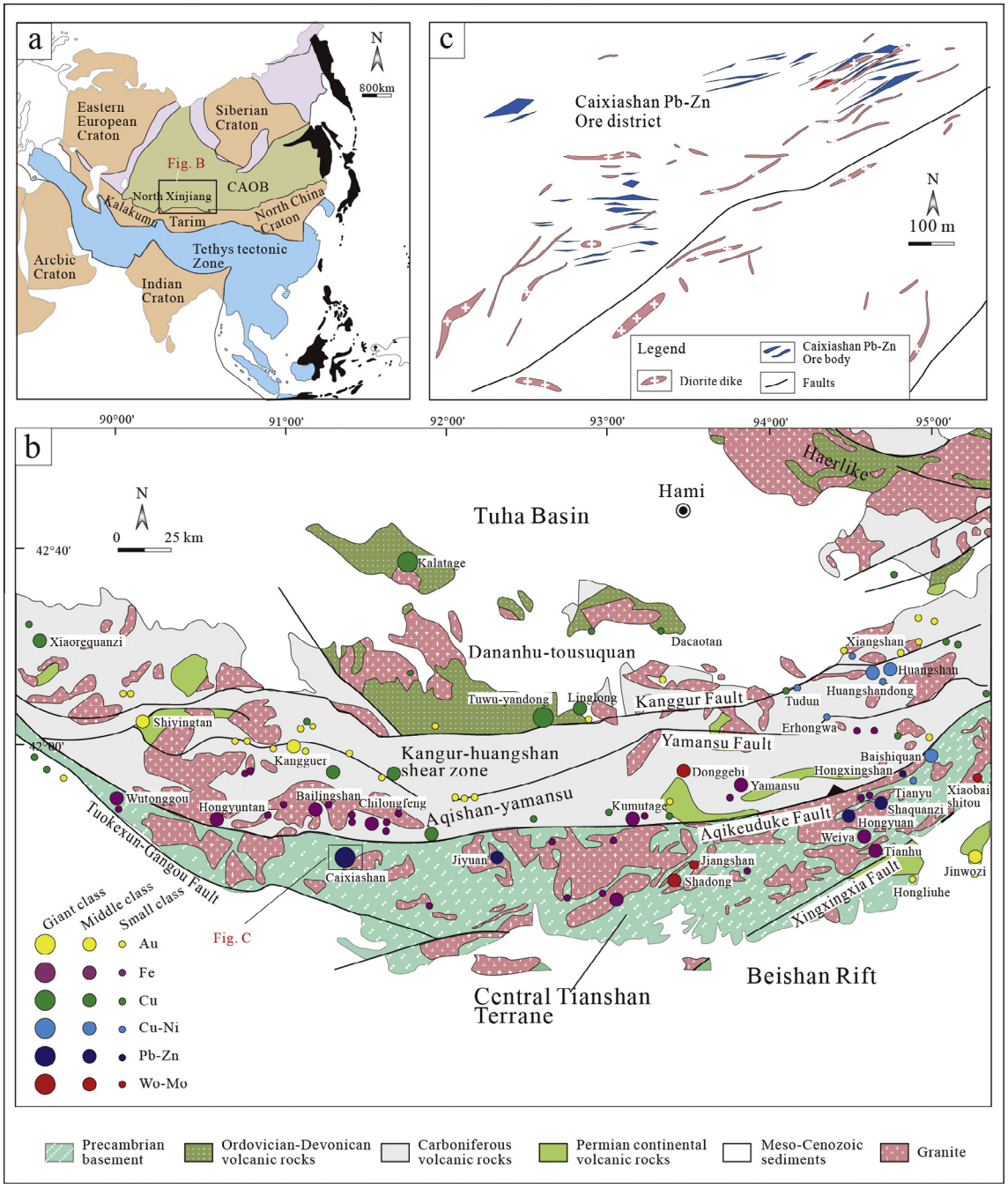

Fig. 1. (a) Simplified tectonic divisions of the CAOB (after Tang et al., 2010a). (b) Geological map of the Eastern Tianshan with emphasis on the distribution of arc-related intrusive rocks of Devonian-Carboniferous age (modified after Xiao et al., 2004). (c) Geological map the of the Caixiashan Pb–Zn ore district showing the location and distribution of the doirite dikes.

previously unstudied diorites from the Eastern Tianshan, to investigate their petrogenesis and tectonic implications.

2. Regional geology and distribution of diorite rocks

The Eastern Tianshan can be subdivided into the Central Tianshan Terrane, the Aqishan-Yamansu block, the Kanggur-Huangshan shear zone and the Dananhu-Tousuquan block from south to north, separated by the E–trending Aqikekuduke, Yamansu and Kanggur faults (Fig. 1b; Ma et al., 1993; Wang et al., 1994; Yang et al., 1996; Zhang et al., 2005). The Eastern Tianshan is interpreted to have formed by the subduction and collision of the Junggar (north) and Tarim (south) plates during the Ordovician to the Carboniferous (Allen and Natal'in, 1995; Pirajno et al., 2008).

The Central Tianshan Terrane is located in the southernmost part of the Eastern Tianshan, which is separated from the Tarim Block to the south by the Tuokexun-Gangou and Xingxingxia faults and the Aqishan-Yamansu volcanic basin to the north by the Aqikekuduke Fault (Guo and Li, 1993; Shu et al., 2004, 2011). The Central Tianshan Terrane contains numerous base- and precious-metal deposits and is dominated by a Proterozoic basement with minor amounts of the Early and Late Paleozoic volcano-sedimentary rocks (Chen et al., 2012; Hu et al., 2000; Mao et al., 2008; Pirajno et al., 2008; Qin et al., 2002) and a large number of granitic

intrusions. The basement is composed of the Mesoproterozoic Xingxingxia, Kawabulake and the Neoproterozoic Tianhu groups whereas the granitic intrusions are predominantly Carboniferous in age (Xiao et al., 2009, 2004). The study area is mainly covered by the Mesoproterozoic Kawabulake Group, which is unconformably overlain by the Lower Cambrian Huangshan Formation and conformably underlain by the Mesoproterozoic Xingxingxia Group, comprised of slate, siliceous siltstone, sandstone, shale and phyllite.

The Late Paleozoic magmatism in the study area (Fig. 1b; in the Caixiashan ore district on the southern edge of the Eastern Tianshan) is related to subduction of the South Tianshan Ocean (Carroll et al., 1995; Chen et al., 1999; Dong et al., 2011; Han et al., 2011). Diorite dikes in the Kawabulake Group dip steeply and trend mainly NE with a smaller proportion trending NW similar to the previous studies in the Junggar area (Xu et al., 2008; Zhou et al., 2008). The dikes are highly variable in size but are mostly less than 1 km long and 5 m wide (Fig. 1c), although some dikes can be a few kilometers in length. The majority of the dikes have been intruded into the clastic rocks of the Kawabulake Group with a few emplaced in the Early Carboniferous rocks or granitic plutons. The dikes rarely crosscut each other but are generally deformed and most have undergone slight alteration.

3. Methodology

3.1. Sample descriptions

Dike samples were collected along a ca. 5 km traverse with a central geographic coordinate around E 91°20′, N 41°42′ near the Caixiashan Zn–Pb deposit hosted in the Kawabulake Group (Fig. 2a and b). Samples were selected in the field and in thin section to exclude those with strong alteration and/or weathering.

The diorite samples are dark green (locally white due to weathering), and medium- to coarse-grained. They are comprised of coarse-grained weakly altered plagioclase (~60%), hornblende

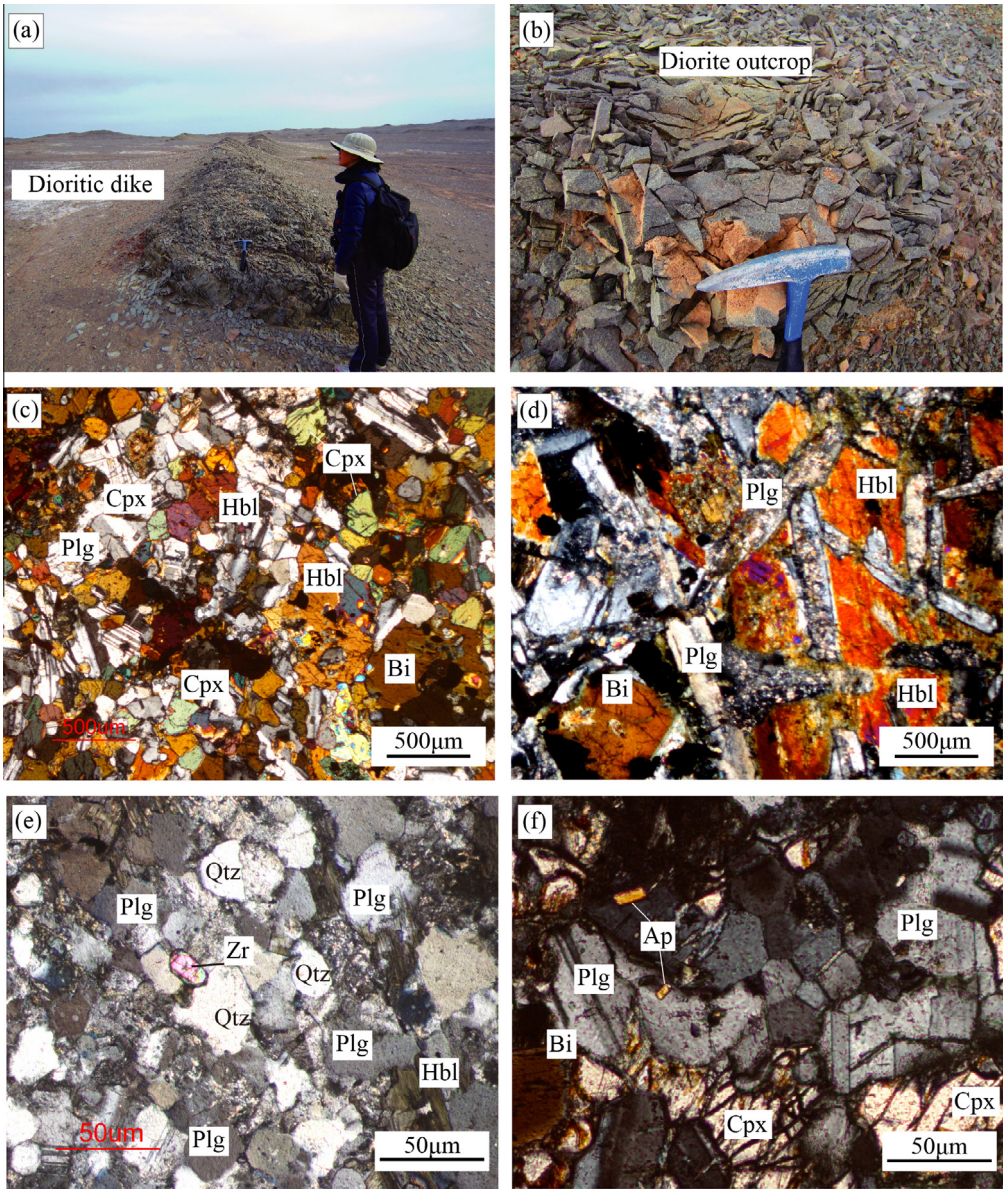

Fig. 2. Representative field photographs and photomicrographs of the rocks analyzed in this study. (a) The dioritic dikes in the field. (b) Photograph showing the location of sample rσ-5. (c) Sample rσ-2, the plagioclase, hornblende, clinopyroxene and biotite in the diorite (crossed nicols). (d) Sample rσ-7, plagioclase, hornblende and small amount of biotite in the diorite (crossed nicols). (e) Sample rσ-9, plagioclase, hornblende, zircon and quartz in the diorite (crossed nicols). (f) Sample rσ-11, plagioclase, clinopyroxene, biotite and apatite in the diorite (crossed nicols).

(~35%) and small amounts of biotite (~5%; Fig. 2c and d). The accessory minerals are zircon and apatite, with minor quartz. Zircon is intergrown with assemblages of hornblende-plagioclase (Fig. 2e) whereas apatite occurs with slightly altered clinopyrox ene-biotite-plagioclase (Fig. 2f).

3.2. Whole rock major and trace elements

Major elements were obtained by X-ray fluorescence spectrometry (XRF) at the ALS Laboratory Group, Guangzhou, using fused lithium tetraborate glass pellets. The analytical precision as determined on the Chinese National standard GSR-3 was generally around 1–5%.

Trace elements, including REE, were determined with a Bruker M90 inductively coupled plasma mass spectrometer (ICP–MS) at the Guizhou Tuopu Resource and Environmental Analysis Center using the method of Qi and Grégoire (2000). Approximately 0.05 grams of powdered sample were placed in a PTFE bomb, and 1 ml of HF and 1 ml of HNO_3 were added. The sealed bombs were then placed in an electric oven and heated to 190 °C for about 36 h. After cooling, the bombs were heated on a hot plate and evaporated to dryness. 500 ng of Rh were added as an internal standard, and then 2 ml of HNO_3 and 4 ml of water were added. The bomb was again sealed and placed in an electric oven at 140 °C for about 5 h to dissolve the residue. After cooling, the final dilution factor was approximately 3000. The sensitivity of the instrument was adjusted to about 5×10^5 cps (counts per second) for 1 ng ml^{-1} of ^{115}In and 2×10^5 cps for 1 ng ml^{-1} of ^{232}Th using the normal sensitivity mode. Pure elemental standards were used for external calibration, and AMH-1 (andesite) and OU-6 (slate) as reference materials. The accuracies of the ICP–MS analyses were better than ±5–10% (relative) for most elements.

3.3. Zircon U–Pb geochronology analyses

After crushing, zircon grains were separated by standard heavy liquid and magnetic techniques. Zircon grains from the N25 μm non-magnetic fractions were hand-picked and mounted with adhesive tape, then enclosed in epoxy resin and polished to about half of their thickness. After being photographed under reflected and transmitted light, the samples were prepared for Cathodoluminescence (CL) imaging and U–Pb dating.

Zircons were photographed under reflected and transmitted light at the State Key Laboratory of Isotope Geochemistry, Guangzhou Institute of Geochemistry.

A GeoLas 2005 Laser Ablation system (Coherent, USA) coupled with an Agilent 7500a ICP-MS and aNu Plasma HR (Wrexham, UK) MC-ICP-MS were employed for in situ zircon U–Pb dating and Lu–Hf isotopic analyses (Yuan et al., 2008), which was undertaken at the State Key Laboratory of Continental Dynamics, Northwest University, Xi'an, China. A pulsed (Geolas) 193 nm ArF Excimer (Lambda Physik, Göttingen Germany) laser energy of 50 mJ/pulse was used for ablation at a repetition rate of 10 Hz with a diameter of 32 μm. Helium was used as a carrier gas to transport the ablated aerosol from the laser-ablation cell to the ICP-MS torch. U–Pb ages showing any detectable common Pb (from the ^{204}Pb count rate) were discarded. The measured ^{204}Pb was used for the common Pb correction using the relevant Pb composition. Analytical procedures followed those described by Yuan et al. (2004). Harvard zircon 91500 was used as an external standard to normalize isotopic fractionation during analysis (Wiedenbeck et al., 2004). The NIST SRM 610 glass was used as an external standard to calculate U, Th, and Pb concentrations of unknowns. Raw data were processed using the GLITTER program (Version 4.4; Jackson et al., 2004) which calculates the relevant isotopic ratios ($^{207}Pb/^{206}Pb$, $^{208}Pb/^{206}Pb$, $^{208}Pb/^{232}Th$, $^{206}Pb/^{238}U$ and $^{207}Pb/^{235}U$ where $^{235}U = {}^{238}U/137.88$) for each mass sweep and displays them as a colored pixel map and as time-resolved intensity traces. GLITTER automatically uses, for each selected ablation time segment of an unknown, the identical integrated ablation time segments of the standard zircon analyses. Then GLITTER corrects the integrated ratios for ablation-related fractionation and instrumental mass bias by calibration against the zircon standard using an interpolative correction (usually linear) for drift in ratios throughout the run, based on the six or more analyses of the standard. It then calculates ratios, ages and errors. A common Pb correction was applied using the method of Andersen (2002), which has minimal effects on the age results. Uncertainties of individual analyses are reported with 1σ errors; weighted mean ages were calculated at the 2σ confidence level. The data were processed using the ISOPLOT (version 3.0) program (Ludwig, 2003). The standard zir-

Table 1
Major oxide and trace element compositions of the dioritic dikes of the Eastern Tianshan.

Sample	rσ-2	rσ-5	rσ-7	rσ-8	rσ-9	rσ-10	rσ-11
Major (wt.%)							
SiO_2	62.15	59.84	59.63	59.75	59.66	59.97	60.79
Al_2O_3	15.06	15.38	15.71	15.76	15.24	15.74	15.67
Fe_2O_3	0.75	0.74	0.76	0.76	0.80	0.76	0.77
FeO	4.27	4.20	4.32	4.28	4.53	4.30	4.34
MnO	0.08	0.08	0.08	0.09	0.09	0.09	0.08
MgO	3.45	3.71	3.95	4.00	4.15	3.88	3.70
CaO	5.10	6.00	5.96	5.41	5.59	5.26	5.48
TiO_2	0.71	0.63	0.69	0.71	0.68	0.67	0.68
Na_2O	4.03	4.26	4.36	4.09	3.66	4.11	4.04
K_2O	1.21	1.08	0.93	1.32	1.21	1.51	1.02
P_2O_5	0.15	0.16	0.16	0.15	0.15	0.15	0.15
LOI	1.44	1.88	1.58	1.84	1.94	2.00	1.66
Tatal	98.40	97.96	98.13	98.16	97.70	98.44	98.38
Mg#	56	58	59	59	59	59	57
Trace (ppm)							
Li	6.47	5.41	6.38	8.08	8.16	7.97	8.15
Be	1.10	1.16	1.21	1.20	1.22	1.32	1.27
Sc	17.4	17.6	18.4	18	17.8	18.2	17.3
V	117	113	117	118	115	110	112
Cr	97.1	99.4	109.0	116.0	117.0	117.0	104.0
Co	18.3	17.6	19.1	17.7	19.9	18.7	17.5
Ni	56.6	64.0	70.4	63.9	65.8	65.3	62.8
Cu	46.7	28.0	8.88	21.0	26.7	25.4	34.2
Zn	65.7	66.4	68.8	56.1	66.0	66.4	59.7
Ga	18.3	19.4	19.4	19.3	18.6	18.4	19.5
Rb	28.0	24.2	22.7	38.5	28.4	42.0	25.8
Sr	561	628	644	639	582	614	593
Y	16.9	17.1	16.2	16.9	18.1	17.2	17.0
Zr	76.4	48.0	57.6	71.7	72.4	68.3	76.8
Nb	5.13	4.27	4.06	4.91	5.03	4.94	4.94
Cs	0.82	0.62	0.77	1.36	0.64	0.89	1.32
Ba	235	242	206	223	226	242	203
Hf	2.10	1.49	1.64	2.09	2.10	2.04	2.21
Ta	0.74	0.32	0.31	0.42	0.36	0.40	0.37
Pb	9.43	8.98	10.50	6.51	8.80	8.65	8.11
Th	3.38	2.30	3.03	3.65	4.24	4.14	4.37
U	0.95	0.88	1.06	0.95	1.24	0.82	0.84
La	16.4	17.7	16.3	15.4	17.2	17.3	17.2
Ce	36.3	37.1	33.8	34.5	37.2	35.9	35.3
Pr	4.48	4.67	4.29	4.22	4.49	4.44	4.47
Nd	18.5	18.3	17.5	17.3	18.4	16.9	17.5
Sm	3.95	4.01	3.74	3.78	3.97	3.67	3.67
Eu	1.06	1.05	1.09	1.10	1.04	1.05	1.05
Gd	3.25	3.41	3.13	3.21	3.39	3.12	2.95
Tb	0.59	0.60	0.56	0.58	0.61	0.57	0.58
Dy	2.99	3.00	2.83	3.00	3.11	2.95	2.98
Ho	0.59	0.60	0.56	0.60	0.62	0.59	0.60
Er	1.73	1.75	1.66	1.76	1.82	1.73	1.73
Tm	0.24	0.24	0.23	0.24	0.25	0.24	0.24
Yb	1.56	1.58	1.48	1.56	1.66	1.58	1.57
Lu	0.23	0.23	0.22	0.23	0.24	0.23	0.23
Sr/Y	33	37	40	38	32	36	35

cons 91500 and GJ-1 yielded weighted average $^{206}Pb/^{238}U$ ages of 1062 ± 5.6 Ma (2σ) and 604.8 ± 2.4 Ma (2σ), respectively, in good agreement with the recommended ages (Jackson et al., 2004; Wiedenbeck et al., 1995; Wiedenbeck et al., 2004).

3.4. Zircon Lu-Hf isotopes

In situ zircon Lu-Hf isotopic measurements were completed at the State Key Laboratory of Continental Dynamics, Northwest University, Xi'an, China, using a Nu Plasma Multi-Collector (MC)-ICP-MS instrument, equipped with a 193 nm ArF Laser Ablation system. The analytical protocol followed that established by Yuan et al. (2008). The analyses were conducted with a spot size of 44 μm, an 8 Hz repetition rate and laser energy of 50 mJ/pulse. Interference of ^{176}Lu on ^{176}Hf was corrected by measuring the intensity of the interference-free ^{175}Lu, using the recommended $^{176}Lu/^{175}Lu$ ratio of 0.02669 to calculate $^{176}Lu/^{177}Hf$ (De Bievre and Taylor, 1993). The isobaric interference of ^{176}Yb on ^{176}Hf was corrected using a recommended $^{176}Yb/^{172}Yb$ ratio of 0.5886 (Chu et al., 2002) to calculate $^{176}Hf/^{177}Hf$ ratios. Zircon 91500 was used as the reference standard for calibration and controlling the condition of analytical instrumentation (Woodhead et al., 2004). The obtained $^{176}Hf/^{177}Hf$ ratio was 0.282296 ± 0.000050 (2σ) for 91500 and 0.282019 ± 15 (2σ) for GJ-1, which is in good agreement with the recommended $^{176}Hf/^{177}Hf$ ratios of 0.2823075 ± 0.0000058 (2σ) for 91500 and 0.282015 ± 0.000019 (2σ) for GJ-1 (Elhlou et al., 2006; Wu et al., 2006).

The decay constant for ^{176}Lu of 1.867 × 10^{-11} $year^{-1}$ was used (Söderlund et al., 2004). The initial $^{176}Hf/^{177}Hf$ ratio, denoted as $\varepsilon Hf(t)$, was calculated relative to the chondritic reservoir with a $^{176}Hf/^{177}Hf$ ratio of 0.282772 and $^{176}Lu/^{177}Hf$ of 0.0332 (Blichert-Toft and Albarède, 1997). Single-stage Hf model ages (T_{DM1}) were calculated relative to the depleted mantle with a present day $^{176}Hf/^{177}Hf$ ratio of 0.28325 and $^{176}Lu/^{177}Hf$ of 0.0384), and two-stage Hf model ages (T_{DM2}) was calculated assuming a mean $^{176}Lu/^{177}Hf$ value of 0.0093 for the average upper continental crust (Vervoort et al., 1996; Vervoort and Blichert-Toft, 1999)

3.5. Whole rock Sr–Nd–Pb isotopes

The whole-rock Sr–Nd isotopic compositions were measured at the Guizhou Tuopu Resource and Environmental Analysis Center using the method of Qi et al. (2000). Chemical separation was undertaken by conventional ion-exchange techniques. About 50 mg of powdered sample was placed in a PTFE bomb, and then 1 ml of HF and 1 ml of HNO_3 were added. The sealed bombs were placed in an electric oven and heated to 185 °C for at almost 36 h.

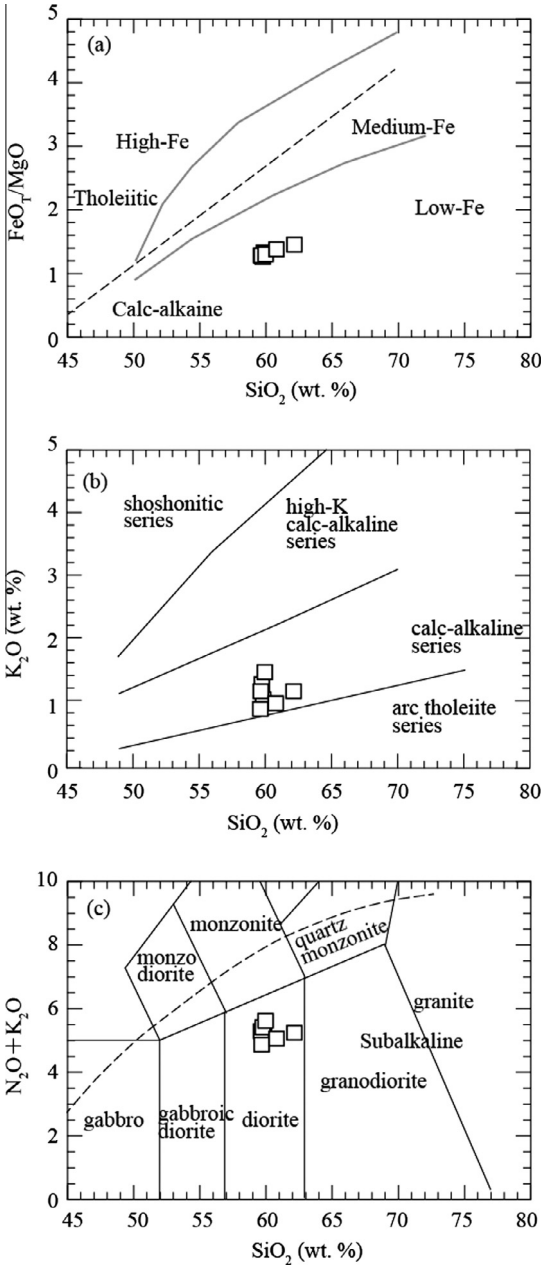

Fig. 3. Discrimination diagrams for the dioritic dikes. (a) SiO_2 versus FeO_T/MgO diagrams (modified after Tang et al., 2010a; and references therein). (b) SiO_2–K_2O plot (Peccerillo and Taylor, 1976). (c) SiO_2–K_2O + Na_2O plot (Middlemost, 1994).

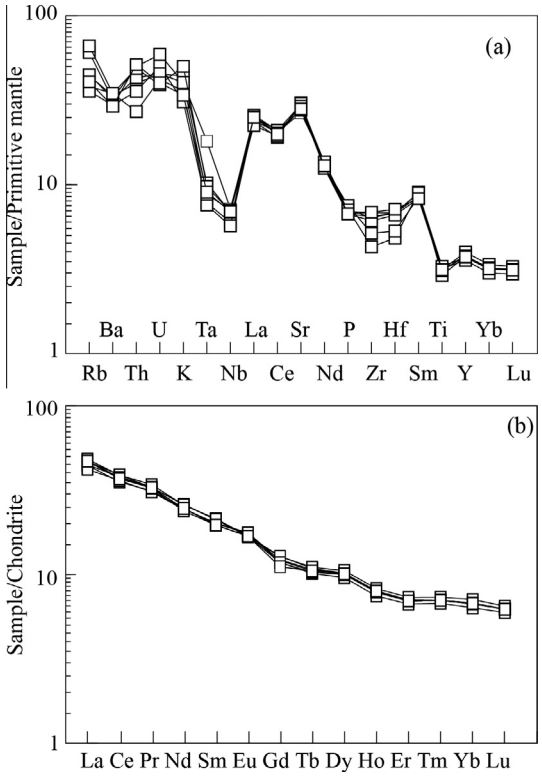

Fig. 4. (a) Primitive mantle normalized spider diagram for the high-Mg dioritic dikes. Normalizing values from Sun and McDonough (1989). (b) Chondrite normalized rare earth element pattern diagram for the high-Mg dioritic dikes. Normalizing values from Taylor and McLennan (1985).

Table 2
Results of U–Pb zircon dating for the doiritic rock of the Eastern Tianshan.

Spot				Isotopic ratios						Calculated ages Ma					
No.	Pb	Th	U	$^{207}Pb/^{206}Pb$	1σ	$^{207}Pb/^{235}U$	1σ	$^{206}Pb/^{238}U$	1σ	$^{207}Pb/^{206}Pb$	1σ	$^{207}Pb/^{235}U$	1σ	$^{206}Pb/^{238}U$	1σ
rσ-2															
1	20	114	156	0.05992	0.00320	0.45468	0.02316	0.05617	0.00086	611	121	381	16	352	5
2	23	139	168	0.05994	0.00345	0.47416	0.03159	0.05635	0.00074	611	124	394	22	353	5
3	18	101	144	0.05146	0.00195	0.39465	0.01471	0.05624	0.00071	261	87	338	11	353	4
4	38	252	250	0.05111	0.00226	0.39606	0.01833	0.05636	0.00076	256	104	339	13	353	5
5	35	203	285	0.05514	0.00288	0.42397	0.02147	0.05621	0.00069	417	117	359	15	353	4
6	34	219	226	0.05233	0.00263	0.39838	0.01910	0.05619	0.00080	298	110	340	14	352	5
7	25	149	177	0.05209	0.00206	0.40225	0.01655	0.05629	0.00066	300	89	343	12	353	4
8	23	143	173	0.05579	0.00248	0.42789	0.01923	0.05626	0.00066	443	98	362	14	353	4
9	46	305	294	0.05665	0.00276	0.42405	0.01958	0.05600	0.00132	480	109	359	14	351	8
10	27	167	190	0.05811	0.00240	0.44767	0.01924	0.05604	0.00083	600	89	376	13	351	5
11	27	157	197	0.05539	0.00402	0.41588	0.02626	0.05606	0.00113	428	163	353	19	352	7
12	35	224	232	0.05592	0.00213	0.43133	0.01725	0.05620	0.00074	450	85	364	12	352	4
13	21	127	166	0.05489	0.00296	0.41981	0.02251	0.05620	0.00071	409	120	356	16	353	4
rσ-7															
1	110	611	1013	0.05450	0.00111	0.42052	0.00972	0.05614	0.00059	391	44	356	7	352	4
2	2339	11,771	21,545	0.05670	0.00040	0.43959	0.00597	0.05617	0.00036	480	15	370	4	352	2
3	193	1173	1716	0.05551	0.00094	0.42756	0.00887	0.05613	0.00075	432	42	361	6	352	5
4	302	1609	2823	0.05510	0.00075	0.42687	0.00950	0.05605	0.00069	417	34	361	7	352	4
5	786	3985	8111	0.05427	0.00142	0.41963	0.01343	0.05597	0.00064	383	59	356	10	351	4
6	2433	14,454	20,535	0.05375	0.00060	0.41590	0.00652	0.05608	0.00039	361	21	353	5	352	2
7	306	1538	2695	0.07078	0.01531	0.42824	0.00954	0.05603	0.00099	951	454	362	7	351	6
8	2328	11,631	22,343	0.05368	0.00034	0.41639	0.00546	0.05606	0.00026	367	15	353	4	352	2
9	5242	35,409	38,166	0.05478	0.00026	0.42475	0.00466	0.05612	0.00027	467	9	359	3	352	2
10	1264	8562	9897	0.05638	0.00055	0.44174	0.01099	0.05620	0.00081	478	22	371	8	352	5
11	1091	5380	10,612	0.05595	0.00048	0.43446	0.00650	0.05610	0.00039	450	23	366	5	352	2
12	6500	41,392	52,560	0.05061	0.00015	0.39389	0.00743	0.05624	0.00031	233	7	337	5	353	2
13	603	5036	3813	0.05979	0.00070	0.46553	0.01758	0.05619	0.00149	594	26	388	12	352	9
rσ-9															
1	161	974	1796	0.05550	0.00118	0.42552	0.01303	0.05553	0.00094	432	48	360	9	348	6
2	149	874	1446	0.05585	0.00090	0.42769	0.00941	0.05541	0.00059	456	37	362	7	348	4
3	397	2317	3551	0.06023	0.00091	0.45992	0.00810	0.05542	0.00043	613	27	384	6	348	3
4	54	326	504	0.05745	0.00155	0.43996	0.01241	0.05560	0.00037	509	56	370	9	349	2
5	87	463	975	0.05486	0.00113	0.41836	0.01103	0.05538	0.00079	406	46	355	8	347	5
6	173	904	1850	0.05289	0.00078	0.40797	0.01029	0.05550	0.00079	324	33	347	7	348	5
7	72	475	688	0.05116	0.00125	0.39152	0.01038	0.05546	0.00047	256	56	335	8	348	3
8	44	263	483	0.05244	0.00150	0.40162	0.01221	0.05561	0.00056	306	65	343	9	349	3
9	128	748	1399	0.05276	0.00090	0.40464	0.00928	0.05557	0.00051	317	44	345	7	349	3
10	100	573	1158	0.05148	0.00089	0.39566	0.00996	0.05554	0.00053	261	34	338	7	348	3
11	159	965	1667	0.05865	0.00305	0.44239	0.02563	0.05543	0.00092	554	115	372	18	348	6
12	230	2013	1793	0.05678	0.00118	0.43693	0.01463	0.05546	0.00061	483	46	368	10	348	4
13	232	1219	1854	0.05410	0.00095	0.41552	0.00990	0.05546	0.00068	376	34	353	7	348	4
14	241	745	2936	0.05645	0.00073	0.43435	0.01110	0.05560	0.00114	478	28	366	8	349	7
15	74	168	1102	0.05461	0.00102	0.41811	0.00983	0.05549	0.00082	394	43	355	7	348	5
16	110	560	1042	0.05200	0.00128	0.39691	0.01027	0.05539	0.00050	287	57	339	7	348	3
rσ-11															
1	64	356	349	0.0545	0.0018	0.4222	0.0145	0.0562	0.0006	391	72.2	358	10.3	352	4
2	57	318	304	0.0533	0.0017	0.4163	0.0152	0.0562	0.0006	343	39.8	353	10.9	352	4
3	49	260	269	0.0542	0.0021	0.4187	0.0164	0.0562	0.0006	389	82.4	355	11.7	352	4
4	52	264	297	0.0494	0.0019	0.3834	0.0159	0.0561	0.0007	165	90.7	330	11.7	352	4
5	52	281	286	0.0535	0.0018	0.4149	0.0158	0.0562	0.0008	346	50.0	352	11.4	353	5
6	64	357	350	0.0581	0.0020	0.4492	0.0168	0.0561	0.0006	600	77.8	377	11.8	352	4
7	60	318	327	0.0522	0.0023	0.4082	0.0212	0.0561	0.0007	295	104	348	15.3	352	4
8	46	253	249	0.0556	0.0021	0.4268	0.0165	0.0562	0.0008	435	83.3	361	11.7	353	5
9	30	149	186	0.0524	0.0027	0.4030	0.0217	0.0562	0.0008	302	114	344	15.7	353	5
10	38	200	223	0.0579	0.0025	0.4446	0.0196	0.0560	0.0007	528	94.4	374	13.8	351	4

The bombs were heated on a hot plate to evaporate to dryness. After cooling. 0.5 ml HCl was added and evaporated to dryness, and then 4 ml of 1.5 mol L^{-1} of HCl was added. The bomb was again sealed and placed in an electric oven at 125 °C for about 5 h to dissolve the residue. The solution was centrifuged at 4×10^3 rpm for 5 min and the supernatant was loaded onto pre-conditioned Dowex 50 W × 8 cation exchange resin columns (8×10^2 mm) for separation of sample matrix and Sr from Rb using 1.5 mol L^{-1} of HCl. Light REE (LREE) was eluted with 6 ml of 6 mol L^{-1} of HCl. The solution was evaporated to dryness and dissolved in 1 ml of 0.25 mol L^{-1} of HCl. The solution was loaded onto the pre-conditioned Ln resin columns for separation of Nd from La, Ce, Pr and Sm. A Neptune MC-ICP-MS was used to measure the $^{87/86}Sr$ and $^{143/144}Nd$ isotope ratios. NIST SRM-987 and JMC-Nd were used as certified reference standard solutions for $^{87/86}Sr$ and $^{143/144}Nd$ isotopes ratio, respectively. Analyses of NIST SRM-987 gave 0.710210 ± 0.000037 (2SD, n = 14) while the JMC Nd standard gave 0.511106 ± 0.000002 (2SD, n = 8). BCR-1 was used as the reference material.

Lead isotopic analyses were performed at the Analytical Laboratory of the Beijing Research Institute of Uranium Geology, China. Sample powders were dissolved in HF + HNO_3 + HClO. Digested samples were dried and redissolved in 6N HCl, dried again and redissolved in 0.5N HBr for Pb separation. The Pb fraction was sep-

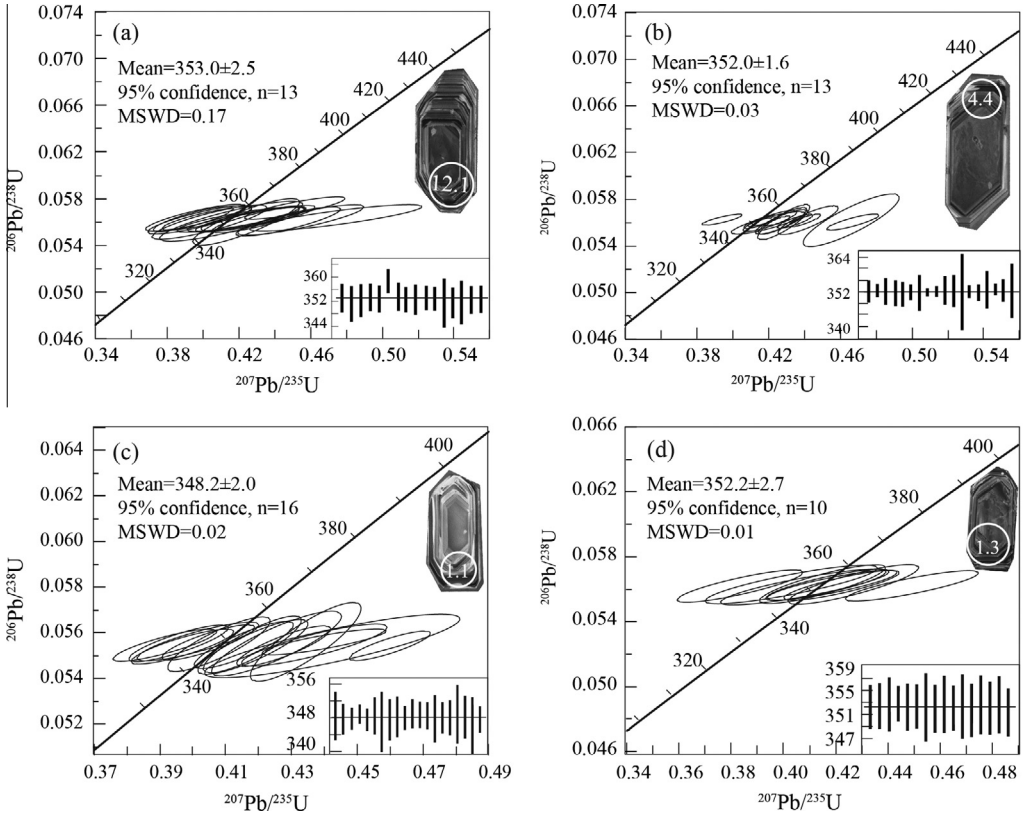

Fig. 5. Representative zircon CL images and U–Pb ages of the diorite samples in the Kawabulake Group in the Eastern Tianshan.

arated using strong alkali anion exchange resin with HBr and HCl as eluents. A factor of 1‰ per mass unit for instrumental mass fractionation was applied to the Pb analyses, using NBS 981 as reference material. Measurement of the common-lead standard NBS 981 gave average values of $^{208}Pb/^{206}Pb = 2.1681 \pm 0.0008$; $^{207}Pb/^{206}Pb = 0.91464 \pm 0.00033$; and $^{204}Pb/^{206}Pb = 0.059042 \pm 0.000037$ with uncertainties of <0.1% at the 95% confidence level.

The $(^{87}Sr/^{86}Sr)_i$, $\varepsilon Nd(t)$, $T_{DM1}(Nd)$ and $T_{DM2}(Nd)$ values used here were calculated based on the method of Wu et al. (2005). The $(^{206}Pb/^{204}Pb)_i$, $(^{207}Pb/^{204}Pb)_i$ and $(^{208}Pb/^{204}Pb)_i$ represent initial Pb isotopic ratios when the rock formed, and was calculated using the Geokit program (Lu, 2004). Ages of these samples used for calculation are given in Section 4.2.

4. Results

4.1. Whole rock major and trace elements geochemistry

The samples contain intermediate SiO_2 (60–62 wt.%), and TiO_2 (0.63–0.71 wt.%) with relatively high Al_2O_3 (15.1–15.8 wt.%), typical of intermediate rocks. The rocks are characterized by high MgO contents (3.45–4.15 wt.%), with Mg# ($Mg\# = 100 \times Mg^{2+}/(Mg^{2+} + TFe^{2+})$) generally >58 (56–59) (see Table 1). They are relatively sodium-rich, with high Na_2O/K_2O ratios (2.7–4.7). All samples share similar major element contents with all samples plotting in the calc-alkaline low Fe area (Fig. 3a), and in the medium-K calc-alkaline field (Fig. 3b). All the samples can be classified as diorites (Fig. 3c).

The samples have elevated concentrations of Cr (97–117 ppm) and Ni (57–70 ppm), consistent with the high Mg# values. On primitive mantle normalized spider diagrams (Fig. 4a), the diorites have enriched large iron lithophile elements (LILE) relative to high field strength elements (HFSE). Samples have high Sr (561–644 ppm) and Ba (203–242 ppm) with relatively high Sr/Y (32–40), Ba/Th (46–105) but low K/Rb (294–384) ratios. The HFSE are characterized by low Nb/Ta (7–14) and Zr/Hf (32–36) ratios. All the samples show LREE enrichment and depletion in the HREE (heavy rare earth elements), with $(La/Yb)_N$ ratios between 6.7 and 7.6 with no significant negative Eu/Eu* anomalies (Fig. 4b).

4.2. Zircon U–Pb

Zircon U–Pb results are presented in Table 2. Zircons from samples rσ-2, rσ-7, rσ-9 and rσ-11 have Th contents of 101–305 ppm, 611–41,392 ppm, 168–2316 ppm and 149–356 ppm, and U contents of 144–294 ppm, 1013–52,560 ppm, 483–3551 ppm and 185–350 ppm, respectively, with moderate to high Th/U ratios (0.70–1.03, 0.50–1.32, 0.15–1.22 and 0.80–1.05). LA-ICP-MS analyses of 13 zircons from sample rσ-2 yielded $^{206}Pb/^{238}U$ ages ranging between 351 ± 5 Ma and 359 ± 4 Ma (2σ; Table 2) and form a tight cluster along the concordia line, with a weighted mean $^{206}Pb/^{238}U$ age of 353.0 ± 2.5 Ma (2σ; MSWD = 0.17; Fig. 5a). Thirteen zircon grains from sample rσ-7 yielded ages ranging between 351 ± 6 Ma and 353 ± 2 Ma (2σ; Table 2), with a weighted mean $^{206}Pb/^{238}U$ age of 352.0 ± 1.6 Ma (2σ; MSWD = 0.03; Fig. 5b). Sixteen zircon grains of sample rσ-9 yielded ages between 347 ± 5 Ma and 349 ± 3 Ma (2σ; Table 2), with a weighted mean $^{206}Pb/^{238}U$ age of 348.2 ± 2.0 Ma (2σ; MSWD = 0.02; Fig. 5c). Ten zircon grains of sample rσ-11 yielded ages ranging from 351 ± 4 Ma to 353 ± 5 Ma (2σ; Table 2), with a weighted mean $^{206}Pb/^{238}U$ age of 352.2 ± 2.7 Ma (2σ; MSWD = 0.01; Fig. 5d).

Table 3
Hf isotopic data for zircons from Dortic rocks of the Kawabulake Group in the Eastern Tianshan.

Sample	Age (Ma)	$^{176}Yb/^{177}Hf$	1σ	$^{176}Lu/^{177}Hf$	1σ	$^{176}Hf/^{177}Hf$	1σ	$^{176}Hf/^{177}Hf_i$	εHf(0)	εHf(t)	T_{DM1}	T_{DM2}	$f_{(Lu/Hf)}$
rσ-2													
1	352	0.01322	0.00004	0.000522	0.000001	0.282897	0.000010	0.282766	4.4	12.1	496	586	−0.98
2	353	0.02116	0.00007	0.000815	0.000003	0.282907	0.000012	0.282657	4.8	12.4	487	568	−0.98
3	353	0.02021	0.00006	0.000786	0.000002	0.282866	0.000013	0.282617	3.3	10.9	544	660	−0.98
4	353	0.02131	0.00005	0.000811	0.000002	0.282863	0.000011	0.282640	3.2	10.8	549	668	−0.98
5	353	0.01505	0.00004	0.000600	0.000001	0.282892	0.000007	0.282741	4.2	11.9	505	599	−0.98
6	352	0.00955	0.00005	0.000408	0.000002	0.282885	0.000011	0.282778	4.0	11.7	512	612	−0.99
7	353	0.01486	0.00002	0.000580	0.000001	0.282830	0.000012	0.282687	2.0	9.7	592	739	−0.98
8	353	0.01460	0.00005	0.000572	0.000002	0.282829	0.000013	0.282613	2.0	9.7	593	741	−0.98
9	351	0.02051	0.00010	0.000798	0.000003	0.282875	0.000011	0.282650	3.6	11.2	532	641	−0.98
10	351	0.01635	0.00002	0.000641	0.000001	0.282833	0.000013	0.282603	2.2	9.8	588	733	−0.98
11	352	0.01971	0.00004	0.000758	0.000001	0.282963	0.000015	0.282753	6.8	14.3	407	440	−0.98
12	352	0.01456	0.00001	0.000576	0.000000	0.282917	0.000015	0.282772	5.1	12.7	470	542	−0.98
13	353	0.01587	0.00001	0.000617	0.000000	0.282928	0.000013	0.282775	5.5	13.1	455	517	−0.98
rσ-7													
1	352	0.04493	0.00018	0.001731	0.000007	0.282759	0.000010	0.282259	−0.5	6.9	713	917	−0.95
2	352	0.17836	0.00089	0.006751	0.000032	0.282937	0.000018	0.280965	5.8	12.0	527	589	−0.80
3	352	0.03211	0.00016	0.001300	0.000006	0.282748	0.000008	0.282392	−0.8	6.6	719	934	−0.96
4	352	0.05748	0.00010	0.002272	0.000004	0.282794	0.000010	0.282130	0.8	8.0	672	846	−0.93
5	351	0.07785	0.00013	0.003020	0.000004	0.282899	0.000011	0.282048	4.5	11.5	528	619	−0.91
6	352	0.03905	0.00040	0.001556	0.000018	0.282741	0.000011	0.282301	−1.1	6.3	735	954	−0.95
7	351	0.05601	0.00031	0.002121	0.000011	0.282813	0.000012	0.282221	1.5	8.7	641	801	−0.94
8	352	0.02809	0.00016	0.001177	0.000007	0.282507	0.000014	0.282189	−9.4	−1.9	1059	1476	−0.96
9	352	0.01803	0.00007	0.000817	0.000004	0.282565	0.000012	0.282359	−7.3	0.3	967	1340	−0.98
10	352	0.05065	0.00016	0.001894	0.000006	0.282779	0.000012	0.282203	0.2	7.5	687	875	−0.94
11	352	0.05226	0.00079	0.002000	0.000029	0.282861	0.000013	0.282288	3.2	10.4	569	689	−0.94
12	353	0.01827	0.00011	0.000706	0.000004	0.282839	0.000015	0.282592	2.4	10.0	581	721	−0.98
13	352	0.01506	0.00015	0.000600	0.000006	0.282897	0.000009	0.282741	4.4	12.1	497	587	−0.98
rσ-9													
1	348	0.04675	0.00033	0.001795	0.000012	0.282782	0.000009	0.282472	0.3	7.6	681	869	−0.95
2	348	0.04064	0.00013	0.001623	0.000005	0.282700	0.000011	0.282299	−2.6	4.7	795	1051	−0.95
3	348	0.04755	0.00016	0.001957	0.000005	0.282779	0.000011	0.282212	0.3	7.5	688	877	−0.94
4	349	0.05110	0.00017	0.001969	0.000006	0.282802	0.000013	0.282265	1.1	8.3	655	825	−0.94
5	347	0.02477	0.00005	0.001003	0.000002	0.282742	0.000009	0.282269	−1.1	6.3	723	948	−0.97
6	348	0.03138	0.00020	0.001275	0.000007	0.282780	0.000010	0.282432	0.3	7.7	674	865	−0.96
7	348	0.02823	0.00007	0.001273	0.000003	0.282866	0.000011	0.282548	3.3	10.7	552	671	−0.96
8	349	0.02165	0.00007	0.000906	0.000002	0.282701	0.000014	0.282448	−2.5	4.9	779	1038	−0.97
9	349	0.03636	0.00021	0.001558	0.000009	0.282975	0.000017	0.282612	7.2	14.5	398	427	−0.95
10	348	0.04825	0.00006	0.001872	0.000002	0.282758	0.000014	0.282234	−0.5	6.7	717	924	−0.94
11	348	0.05835	0.00045	0.002264	0.000016	0.282805	0.000013	0.282170	1.2	8.3	656	824	−0.93
12	348	0.03197	0.00011	0.001375	0.000005	0.282641	0.000013	0.282335	−4.7	2.7	874	1181	−0.96
13	348	0.05056	0.00051	0.001954	0.000017	0.282770	0.000017	0.282172	−0.1	7.1	701	898	−0.94
14	349	0.00806	0.00003	0.000348	0.000001	0.282366	0.000011	0.282279	−14.3	−6.8	1229	1781	−0.99
15	348	0.09486	0.00021	0.003660	0.000008	0.282973	0.000013	0.281948	7.1	13.9	425	463	−0.89
16	348	0.03854	0.00009	0.001531	0.000004	0.282750	0.000011	0.282328	−0.8	6.5	722	937	−0.95
rσ-11													
1	352	0.02290	0.00010	0.000852	0.000004	0.282808	0.000025	0.282432	1.3	8.8	627	793	−0.97
2	352	0.03542	0.00019	0.001317	0.000007	0.282916	0.000028	0.282480	5.1	12.5	481	556	−0.96
3	352	0.01581	0.00004	0.000587	0.000001	0.282825	0.000033	0.282624	1.9	9.5	598	750	−0.98
4	352	0.01615	0.00018	0.000629	0.000007	0.282869	0.000012	0.282723	3.4	11.0	537	651	−0.98
5	353	0.02787	0.00004	0.001028	0.000002	0.282899	0.000021	0.282651	4.5	12.0	500	588	−0.97
6	352	0.01570	0.00002	0.000622	0.000001	0.282822	0.000009	0.282634	1.8	9.4	604	759	−0.98
7	352	0.02744	0.00025	0.001049	0.000009	0.282911	0.000011	0.282541	4.9	12.4	483	562	−0.97
8	353	0.01874	0.00003	0.000735	0.000001	0.282891	0.000015	0.282692	4.2	11.8	507	602	−0.98
9	353	0.02203	0.00015	0.000836	0.000005	0.282905	0.000012	0.282648	4.7	12.3	489	572	−0.97
10	351	0.02482	0.00015	0.000953	0.000006	0.282809	0.000015	0.282476	1.3	8.8	627	792	−0.97

4.3. Zircon Lu-Hf isotopes

Zircons from the diorite samples have variable Hf isotopic compositions with $^{176}Hf/^{177}Hf$ ratios ranging from 0.282366 to 0.282975, $\varepsilon Hf(t)$ values range from −6.8 to +14.5. The Hf model ages of T_{DM1} and T_{DM2} range from 0.4 to 1.2 Ga and 0.4 to 1.8 Ga, respectively (Table 3; Fig. 6).

4.4. Whole rock Sr–Nd–Pb isotopes

Whole-rock Sr–Nd–Pb isotopic compositions of the dioritic rocks in the Kawabulake Group are presented in Table 4. The samples have uniform isotopic compositions with $^{87}Rb/^{86}Sr$ values of 0.111 and 0.174, and initial $^{87}Sr/^{86}Sr$ ratio values of 0.704299 and 0.705113. They have variable $\varepsilon Nd(t)$ values of −5.2 to +2.2, and $T_{DM2}(Nd)$ range from 0.93 Ga to 1.53 Ga. The $(^{206}Pb/^{204}Pb)_i$, $(^{207}Pb/^{204}Pb)_i$ and $(^{208}Pb/^{204}Pb)_i$ of the dioritic dikes are 17.953–18.077, 15.466–15.502, 37.566–37.798, respectively (Table 4).

5. Discussion

5.1. The link with HMA

The high-Mg diorites are characterized by intermediate SiO_2, high MgO, high Cr (97–117 ppm) and Ni (57–70 ppm) contents, strong Nb and Ta depletions, high Sr and Ba, and highly fractionated

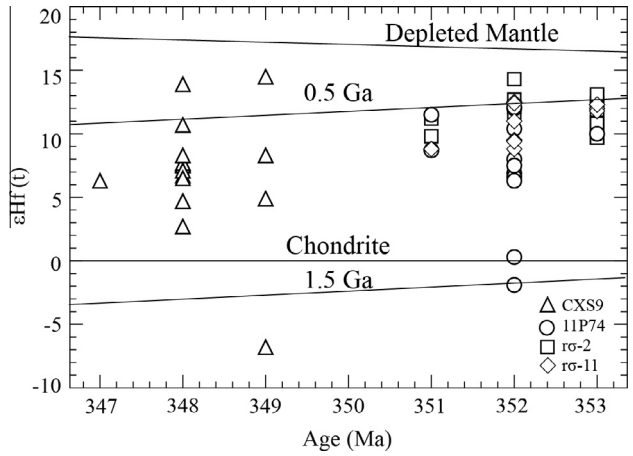

Fig. 6. $\varepsilon Hf(t)$ versus age of the dioritic dikes in the Kawabulake Group.

Table 4
The Sr, Nd and Pb isotopic composition of the diorite samples.

Sample	rσ-2	rσ-7	rσ-8	rσ-9	rσ-11
Sr–Nd					
Rb	28.0	24.2	38.5	28.4	25.8
Sr	561	628	639	582	593
$^{87}Rb/^{86}Sr$	0.144	0.111	0.174	0.141	0.126
$^{87}Sr/^{86}Sr$	0.705037	0.704856	0.705583	0.705818	0.705351
$(^{87}Sr/^{86}Sr)_i$	0.704315	0.704299	0.704712	0.705113	0.704722
Sm	3.95	4.01	3.78	3.97	3.67
Nd	18.5	18.3	17.3	18.4	17.5
$^{147}Sm/^{144}Nd$	0.1292	0.1326	0.1322	0.1305	0.1269
$^{143}Nd/^{144}Nd$	0.512358	0.512224	0.512471	0.512596	0.512397
$f_{Sm/Nd}$	−0.34	−0.33	−0.33	−0.34	−0.35
$(^{143}Nd/^{144}Nd)_i$	0.512060	0.511918	0.512166	0.512295	0.512105
$\varepsilon Nd(t)$	−2.4	−5.2	−0.4	2.2	−1.6
T_{DM1}	1426	1736	1269	1016	1320
T_{DM2}	1301	1526	1133	929	1230
Pb					
U	0.95	0.88	0.95	1.24	0.84
Th	3.38	2.30	3.65	4.24	4.37
Pb	9.43	8.98	6.51	8.80	8.11
$^{206}Pb/^{204}Pb$	18.405	18.297	18.488	18.523	18.442
2σ	0.004	0.005	0.009	0.008	0.004
$^{207}Pb/^{204}Pb$	15.485	15.494	15.530	15.498	15.490
2σ	0.003	0.004	0.007	0.007	0.002
$^{208}Pb/^{204}Pb$	38.201	38.057	38.296	38.352	38.184
2σ	0.006	0.009	0.018	0.015	0.005
$(^{206}Pb/^{204}Pb)_i$	18.050	17.953	17.972	18.024	18.077
$(^{207}Pb/^{204}Pb)_i$	15.466	15.476	15.502	15.471	15.470
$(^{208}Pb/^{204}Pb)_i$	37.790	37.764	37.651	37.798	37.566

The Rb, Sr, Sm, Nd, U, Th, and Pb concentrations used in Table 4 are from Table 1.

REEs (Fig. 4). The Mg-numbers (Mg#) are generally higher than >56 similar to those of high-Mg adakites and sanukitoid HMA magmas (Kamei et al., 2004). On the plot of SiO_2 versus MgO designed for distinguishing HMA from normal andesite (McCarron and Smellie, 1998), all the dike samples fall in the HMA field (Fig. 7a), suggesting that the high-Mg diorites are similar to HMAs.

HMAs can be divided into four types, namely adakitic, bajaitic, boninitic and sanukitoid HMA. The dioritic dikes in the Kawabulake Group most closely resemble sanukitoid HMA (Fig. 7b–d). The high TiO_2 contents of the Kawabulake dioritic dikes are not consistent with boninitic HMA that are characterized by low TiO_2, HFSEs, REE and LILE (Fig. 7b; Hickey and Frey, 1982; Taylor et al., 1994). The $(La/Yb)_N < 10$ of the dioritic samples in this study are also distinct from the adakitic and bajaitic HMA ($(La/Yb)_N > 10$; Drummond and Defant, 1990; Rogers et al., 1985; Yogodzinski et al., 1994; Fig. 7c). Diorite samples also show low Sr/Y ratios and high values of Y (Fig. 7d), similar to the sanukitoid HMA but distinct from other HMA subtypes, suggesting they are best classified as sanukitoid HMA.

5.2. Petrogenesis

The enriched LILE and LREE but depleted HREE and negative Nb, Ta, Ti and P anomalies of the diorites (Fig. 4a and b) are typical of subduction-related magmas. The positive $\varepsilon Hf(t)$ values in four samples of the Kawabulake diorites are similar to those of depleted mantle (Fig. 8), an interpretation that is consistent with the positive $\varepsilon Nd(t)$ values and the Pb isotopic compositions (Fig. 9a and b). The fact that the whole rock $\varepsilon Nd(t)$ values are somewhat more negative than the zircon $\varepsilon Hf(t)$ may have been the result of lower closure temperatures in some components in the whole rock samples (plagioclase: 350–400 °C; Grove et al., 1984) than in the zircons (>900 °C; Lee et al., 1997). The geochemistry of the diorite dikes is consistent with them being derived from a depleted mantle source, similar to that proposed for other sanukitoids (Beyth et al., 1994; Heilimo et al., 2010; Martin, 1999; Martin et al., 2009, 2005). The sanukitoid HMA suite is widely considered to be generated through interaction of a mantle peridotite with a silicic melt derived from partial melting of a subducting oceanic slab and/or sediment (e.g., Yogodzinski et al., 1994; Tatsumi, 2001, 2006; Tatsumi and Hanyu, 2003; Tatsumi et al., 2003), consistent with experimental results that show that sanukitoid can be produced by partial melting of harzburgitic or lherzolitic mantle (Tatsumi, 2001; Tatsumi and Ishizaka, 1982).

The $(^{206}Pb/^{204}Pb)_i$ of the dioritic dikes (17.953–18.077) from this study are lower than those of Mid Ocean Ridge Basalt (MORB = 18.275; Workman and Hart, 2005), suggesting that MORB melting was not the direct source for the Kawabulake Group diorite. It is also unlikely that the dioritic dikes in the Kawabulake Group were formed by low-pressure fractional crystallization (AFC) of parental basaltic magma (Castillo, 2006, 2012), as the assumed parental basalt in the study area is characterized by higher Sr–Nd–Pb isotope values (the $\varepsilon Nd(t)$ of Xiaorequanzi basalt a is mostly >3; Xia et al., 2008). The geochemistry of dioritic dikes in the Kawabulake Group is not consistent with the delamination of over thickened lower crust, as magmas derived from the lower crust are commonly characterized by low MgO and Mg# based on experimental results from metabasalts and eclogites (Wang et al., 2006; Fig. 10a and b). The low K contents (0.9–1.3 wt.%) and inhomogeneous $\varepsilon Nd(t)$ values (−6.9 to +2.2) of the diorites is distinct from adakitic rocks formed by partial melting of subducted continental crust in collisional orogenic belts in Tibet (Wang et al., 2008), which are characterized by high K content (>3 wt.%). It is also unlikely that mixing of felsic and basaltic magma can generate the dioritic dikes in the Kawabulake Group, as the plagioclase in the diorites shows normal zoning whereas magma mixing will typically generate complex zoning (Sakuyama, 1981).

The geochemical and isotopic data suggest that the diorite dykes were derived from a depleted mantle source. However, the negative $\varepsilon Hf(t)$ and $\varepsilon Nd(t)$ values indicate that some old crustal material was added to the system (Huang et al., 2011). Modeling was undertaken to test this, using the values of depleted mantle (DM) to represent the mantle source and the Mesoproterozoic Kawabulake Group of Eastern Tianshan to represent the sediment. Based on these starting materials the Sr, Nd and Pb isotopic data show that the dioritic dikes can be generated by mixture ratios (depleted mantle melt to sediment melt) from 95:5 to 98:2 with an average of 97:3 (Fig. 11a and b). This is similar to results for high-Mg dioritic dikes in the W-Junggar which are interpreted to have incorporated ~5% of sediment into the source (Tang et al., 2010a). The inhomogeneous $\varepsilon Hf(t)$ and $\varepsilon Nd(t)$ values suggest that

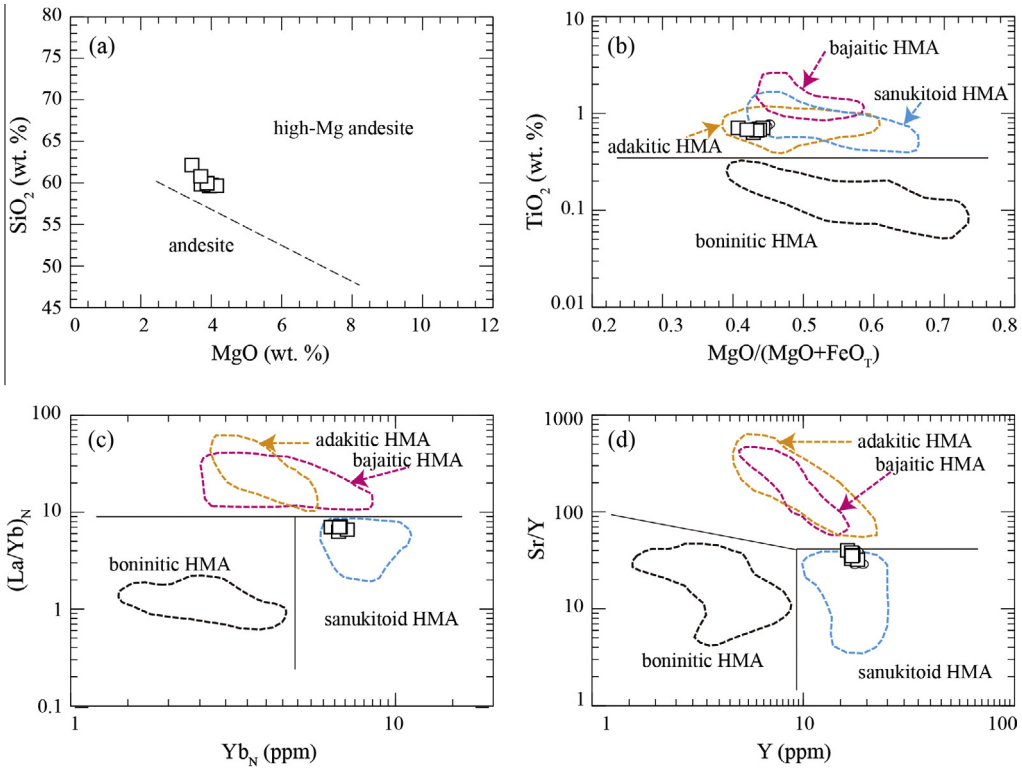

Fig. 7. Classification of tholeiitic and calc-alkaline series with the high-Mg diorites and HMAs using the geochemical system devised by Miyashiro (1974). Previously published data of HMAs are divided into four types namely sanukitoid HMA, adakitic HMA, bajaitic HMA, and boninitic HMA (Kamei et al., 2004).

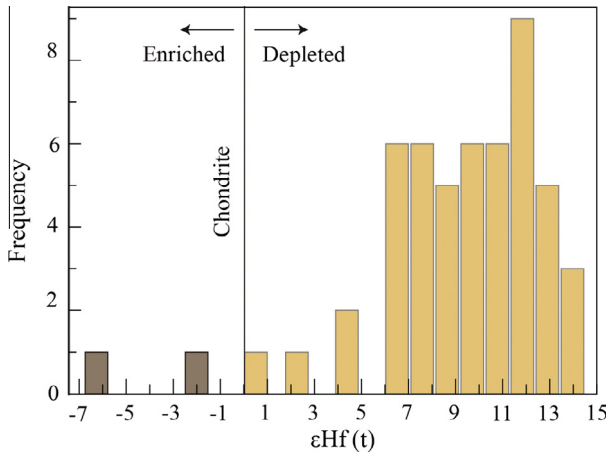

Fig. 8. Histogram for $\varepsilon Hf(t)$ of the dioritic dikes at Kawabulake Group.

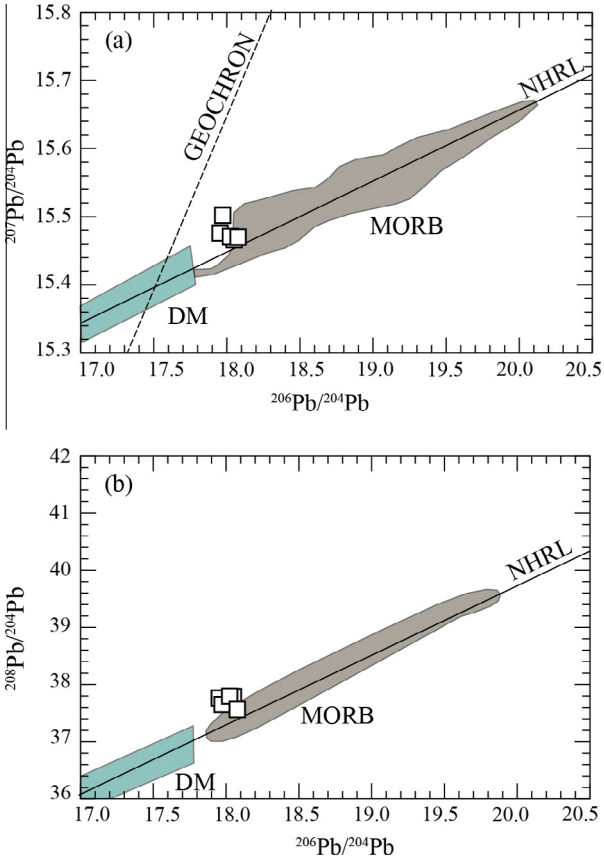

Fig. 9. (a) Diagram of $^{207}Pb/^{204}Pb$ versus $^{206}Pb/^{204}Pb$. (b) Diagram of $^{208}Pb/^{204}Pb$ versus $^{206}Pb/^{204}Pb$. DM, depleted mantle; MORB, mid-ocean ridge basalt; NHRL, northern hemisphere reference line.

the sediment was added during ascent rather than in the source area which would tend to produce more uniform values.

In summary, the geological setting, geochemistry and isotopic characteristics of the dioritic dikes suggest that they were generated by partial melting of mantle wedge that assimilated minor sediment (~3%) during the upwelling process analogous to sanukitoids in Japan (Shimoda et al., 1998; Tatsumi, 2006; Tatsumi and Ishizaka, 1982).

5.3. Tectonic implications for the Eastern Tianshan

High Mg dioritic dike are widely exposed in the Eastern Tianshan (this study), Junggar (Tang et al., 2012a, 2010a, 2012b, 2010b, 2012c; Yin et al., 2010) and Kunlun (Zhang et al., 2014)

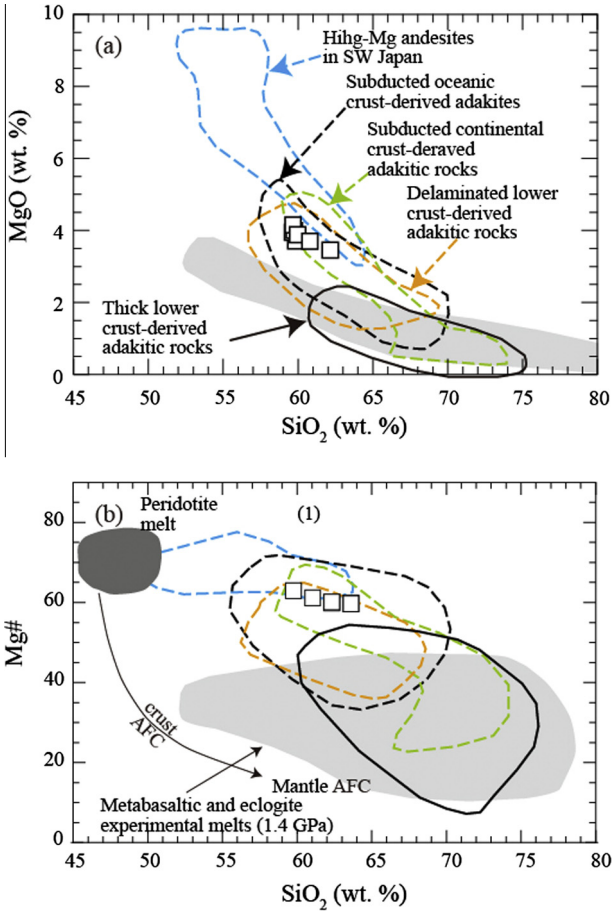

Fig. 10. (a) SiO_2 versus MgO diagram. (b) SiO_2 versus Mg# diagram. The fields are modified after Tang et al. (2010a) and reference therein. Data for metabasaltic and eclogite experimental melts (1–4.0 GPa), and peridotite-hybridized equivalent, are from Rapp et al. (1999) and references therein.

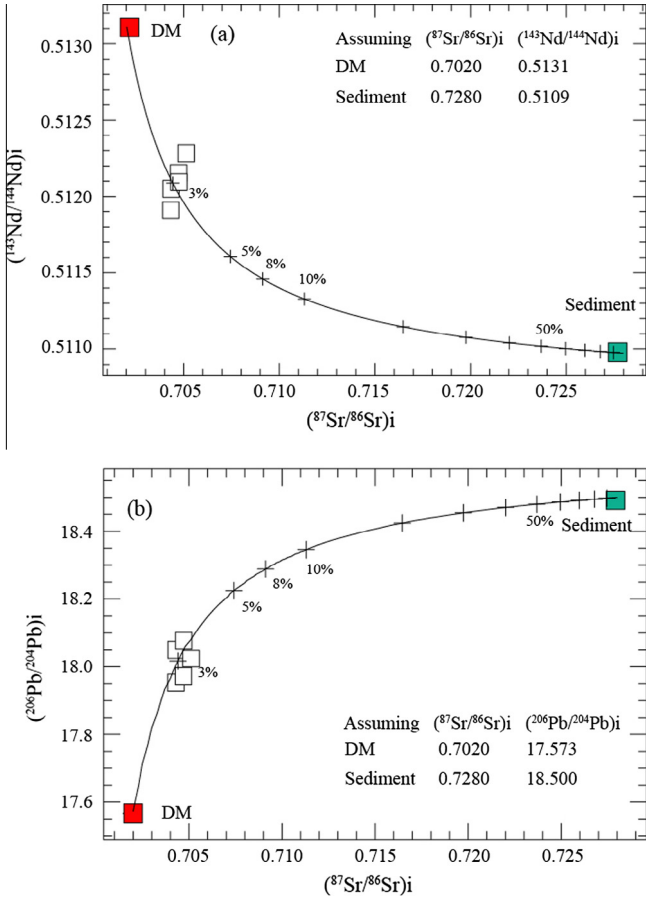

Fig. 11. Simple mixing modeling results of depleted mantle and sediments for the studied rock suites for (a) Sr–Nd, (b) Sr–Pb. The Sr–Nd–Pb isotopic compositions of depleted mantle are from Salters and Stracke (2004) and the sediment are from Li et al. (submitted for publication). The sources of average REEs of sanukitoid (Shimoda et al., 1998; Tatsumi, 2006; Tatsumi and Ishizaka, 1982) and references therein.

areas. Volumetrically important HMA may be produced in certain times and places under favorable tectonic conditions (Kelemen, 1995), with many HMA generated during subduction (Cascades, Baja California, Western Mexico, Southern Chile; Drummond and Defant, 1990; Drummond et al., 1996). As discussed above, the high Mg diorite dikes are likely derived from a subduction-modified mantle source that assimilated sediment during upwelling.

Although subduction zones are generally compressional environments, the linear distribution of these dioritic dikes implies an extensional environment. Episodes of extension in arcs may be caused by processes such as slab detachment, i.e., the detachment of thickened lithospheric mantle from overlying crust during continental collision (Bird, 1978), or slab roll-back (Wortel and Spakman, 2000). However, the widespread Carboniferous granitoids in the Central Tianshan region (Fig. 1b) are not consistent with either model, as both detachment and roll-back will typically generate a narrow, linear zone of magma parallel to the subduction zone (Wilcox et al., 1973; Dewey and Burke, 1974). Moreover, delamination usually results in the foundering of denser lithosphere into less dense asthenosphere, which is more likely to happen during continental collision (Davies and von Blanckenburg, 1995) when the resultant opposing buoyancy forces generate narrow extensional rifts. The near uniform trend of dikes at Eastern Tianshan, together with the younger ages from east to west, suggest that the dikes were likely generated by progressive subduction in the Eastern Tianshan area.

In addition, the presence of the Late Devonian Kawabulake ophiolite mélanges (SHRIMP U–Pb, 377 ± 2 Ma; Xiao et al., 2008) and subduction-related Cu–Au mineralization (Chen and Jahn, 2004; Han et al., 2010) suggest that subduction in the southern edge of Eastern Tianshan was ongoing in the Late Devonian. The tectonic evolution of the Early Carboniferous Eastern Tianshan can be summarized as follows: (1) melts/fluids of the subducted slab matasomatised the lithosphere mantle, generating the mantle-derived magma; (2) these magmas assimilated sedimentary rocks of the Mesoproterozoic Kawabulake Group during ascent to generate the sanukitoid high Mg dioritic dikes ~350 Ma in the Eastern Tianshan area; and (3) melting of the subducted oceanic crust generated the adakitic rocks which host the Tuwuyandong porphyry Cu deposits (~333 Ma; Han et al., 2006; Zhang et al., 2006);

6. Conclusions

Zircon U–Pb ages of 353–348 Ma for the high Mg dioritic dikes from the Eastern Tianshan region in the southwestern part of the CAOB indicate that these intrusions were emplaced in the Early Carboniferous. The dikes are characterized by intermediate SiO_2, low TiO_2, relatively high Al_2O_3 and MgO contents, with Mg# generally higher than 56 (56–59) similar to sanukitoids. Field observations, mineralogical, geochemical, whole rock Sr–Nd and zircon Hf isotopic data suggest that the dioritic dikes were generated by

partial melting of mantle wedge that assimilated minor amounts of sedimentary rocks from the Mesoproterozoic Kawabulake Group during ascent. The sanukitoid-like dioritic dikes and coeval adakite likely reflect a subduction regime, which give rise to the potential Cu–Au mineralization in the area during the Early Carboniferous.

Acknowledgements

This study was financially supported by the Chinese National Basic Research 973-Program (2014CB440802), and the National Natural Science Foundation of China (NSFC) (nos. 41072062 and 40730421). The Office of Project-305, the First Brigade of Xinjiang Geology and Mineral Resources Bureau and Xinjiang Institute of Geological Survey helped our field investigation. Two anonymous reviewers are thanked for constructive reviews that greatly improved the quality of this paper. A normal geologist and beloved brother, Mengjiang Li, is remembered for who lost his life during the fieldwork in 2015. This is contribution No.IS-2114 from GIGCAS.

References

Allen, M., Natal'in, B., 1995. Junggar, Turfan and Alakol basins as Late Permian to? Early Triassic extensional structures in a sinistral shear zone in the Altaid orogenic collage, Central Asia. J. Geol. Soc. 152, 327–338.

Andersen, T., 2002. Correction of common lead in U–Pb analyses that do not report ^{204}Pb. Chem. Geol. 192, 59–79.

Beyth, M., Stern, R.J., Altherr, R., Kröner, A., 1994. The late Precambrian Timna igneous complex, southern Israel: evidence for comagmatic-type sanukitoid monzodiorite and alkali granite magma. Lithos 31, 103–124.

Bird, P., 1978. Initiation of intracontinental subduction in the Himalaya. J. Geophys. Res.: Solid Earth (1978–2012) 83, 4975–4987.

Blichert-Toft, J., Albarède, F., 1997. The Lu–Hf isotope geochemistry of chondrites and the evolution of the mantle-crust system. Earth Planet. Sci. Lett. 148, 243–258.

Carroll, A., Graham, S., Hendrix, M., Ying, D., Zhou, D., 1995. Late Paleozoic tectonic amalgamation of northwestern China: sedimentary record of the northern Tarim, northwestern Turpan, and southern Junggar basins. Geol. Soc. Am. Bull. 107, 571–594.

Castillo, P.R., 2006. An overview of adakite petrogenesis. Chinese Sci. Bull. 51, 257–268.

Castillo, P.R., 2012. Adakite petrogenesis. Lithos 134, 304–316.

Chen, B., Jahn, B.-M., 2004. Genesis of post-collisional granitoids and basement nature of the Junggar Terrane, NW China: Nd–Sr isotope and trace element evidence. J. Asian Earth Sci. 23, 691–703.

Chen, C., Lu, H., Jia, D., Cai, D., Wu, S., 1999. Closing history of the southern Tianshan oceanic basin, western China: an oblique collisional orogeny. Tectonophysics 302, 23–40.

Chen, Y.J., Pirajno, F., Wu, G., Qi, J.P., Xiong, X.L., 2012. Epithermal deposits in North Xinjiang, NW China. Int. J. Earth Sci. 101, 889–917.

Chu, N.C., Taylor, R.N., Chavagnac, V., Nesbitt, R.W., Boella, R.M., Milton, J.A., German, C.R., Bayon, G., Burton, K., 2002. Hf isotope ratio analysis using multi-collector inductively coupled plasma mass spectrometry: an evaluation of isobaric interference corrections. J. Anal. At. Spectrom. 17, 1567–1574.

Davies, J.H., von Blanckenburg, F., 1995. Slab breakoff: a model of lithosphere detachment and its test in the magmatism and deformation of collisional orogens. Earth Planet. Sci. Lett. 129, 85–102.

De Bievre, P., Taylor, P.D.P., 1993. Table of the isotopic compositions of the elements. Int. J. Mass Spectrom. Ion Processes 123, 149–166.

Dewey, J.F., Burke, K., 1974. Hot spots and continental break-up: implications for collisional orogeny. Geology 2, 57–60.

Dong, Y., Zhang, G., Neubauer, F., Liu, X., Hauzenberger, C., Zhou, D., Li, W., 2011. Syn-and post-collisional granitoids in the Central Tianshan orogen: geochemistry, geochronology and implications for tectonic evolution. Gondwana Res. 20, 568–581.

Drummond, M.S., Defant, M.J., 1990. A model for trondhjemite-tonalite-dacite genesis and crustal growth via slab melting: Archean to modern comparisons. J. Geophys. Res.: Solid Earth (1978–2012) 95, 21503–21521.

Drummond, M.S., Defant, M.J., Kepezhinskas, P.K., 1996. Petrogenesis of slab-derived trondhjemite–tonalite-dacite/adakite magmas. Geol. Soc. Am. Spec. Pap. 315, 205–215.

Elhlou, S., Belousova, E., Griffin, W.L., Pearson, N.J., O'reilly, S.Y., 2006. Trace element and isotopic composition of GJ-red zircon standard by laser ablation. Geochim. Cosmochim. Acta 70, A158.

Grove, T.L., Baker, M.B., Kinzler, R.J., 1984. Coupled CaAl–NaSi diffusion in plagioclase feldspar: experiments and applications to cooling rate speedometry. Geochim. Cosmochim. Acta 48, 2113–2121.

Guo, Z., Li, M., 1993. On the Early Paleozoic Dispersed Terranes in Mid-Tianshan. Acta Scicentiarum Naturalum Universitis Pekinesis 3, 009.

Han, B.F., Guo, Z.J., Zhang, Z.C., Zhang, L., Chen, J.F., Song, B., 2010. Age, geochemistry, and tectonic implications of a late Paleozoic stitching pluton in the North Tian Shan suture zone, western China. Geol. Soc. Am. Bull. 122, 627–640.

Han, B.F., He, G.Q., Wang, X.C., Guo, Z.J., 2011. Late Carboniferous collision between the Tarim and Kazakhstan-Yili terranes in the western segment of the South Tian Shan Orogen, Central Asia, and implications for the Northern Xinjiang, western China. Earth Sci. Rev. 109, 74–93.

Han, C., Xiao, W., Zhao, G., Mao, J., Yang, J., Wang, Z., Yan, Z., Mao, Q., 2006. Geological characteristics and genesis of the Tuwu porphyry copper deposit, Hami, Xinjiang, Central Asia. Ore Geol. Rev. 29, 77–94.

Heilimo, E., Halla, J., Hölttä, P., 2010. Discrimination and origin of the sanukitoid series: geochemical constraints from the Neoarchean western Karelian Province (Finland). Lithos 115, 27–39.

Hickey, R.L., Frey, F.A., 1982. Geochemical characteristics of boninite series volcanics: implications for their source. Geochim. Cosmochim. Acta 46, 2099–2115.

Hu, A., Jahn, B.M., Zhang, G., Chen, Y., Zhang, Q., 2000. Crustal evolution and Phanerozoic crustal growth in northern Xinjiang: Nd isotopic evidence. Part I. Isotopic characterization of basement rocks. Tectonophysics 328, 15–51.

Huang, H.Q., Li, X.H., Li, W.X., Li, Z.X., 2011. Formation of high δ^{18}O fayalite-bearing A-type granite by high-temperature melting of granulitic metasedimentary rocks, southern China. Geology 39, 903–906.

Jackson, S.E., Pearson, N.J., Griffin, W.L., Belousova, E.A., 2004. The application of laser ablation-inductively coupled plasma-mass spectrometry to in situ U–Pb zircon geochronology. Chem. Geol. 211, 47–69.

Jahn, B.M., 2004. The Central Asian Orogenic Belt and growth of the continental crust in the Phanerozoic. Geol. Soc. London Spec. Publ. 226, 73–100.

Jahn, B.M., Griffin, W.L., Windley, B., 2000a. Continental growth in the Phanerozoic: evidence from Central Asia. Tectonophysics 328, vii–x.

Jahn, B.M., Wu, F., Chen, B., 2000b. Granitoids of the Central Asian Orogenic Belt and continental growth in the Phanerozoic. Geol. Soc. Am. Spec. Pap. 350, 181–193.

Jahn, B.M., Wu, F., Chen, B., 2000c. Massive granitoid generation in Central Asia: Nd isotope evidence and implication for continental growth in the Phanerozoic. Episodes 23, 82–92.

Kamei, A., Owada, M., Nagao, T., Shiraki, K., 2004. High-Mg diorites derived from sanukitic HMA magmas, Kyushu Island, southwest Japan arc: evidence from clinopyroxene and whole rock compositions. Lithos 75, 359–371.

Kelemen, P.B., 1995. Genesis of high Mg# andesites and the continental crust. Contrib. Miner. Petrol. 120, 1–19.

Lee, J.K.W., Williams, I.S., Ellis, D.J., 1997. Pb, U and Th diffusion in natural zircon. Nature 390, 159–162.

Lu, Y.F., 2004. GeoKit-A geochemical toolkit for Microsoft Excel. Geochimica 33, 459–464.

Ludwig, K.R., 2003. User's Manual for Isoplot 3.00: A Geochronological Toolkit for Microsoft Excel. Berkeley Geochronology Centre Special Publication.

Ma, R., Wang, C., Ye, S., 1993. Tectonic Framework and Crustal Evolution of Eastern Tianshan Mountains. Publishing House of Nanjing University, Nanjing, p. 225 (in Chinese with English abstract).

Mao, J.W., Pirajno, F., Zhang, Z.H., Chai, F.M., Wu, H., Chen, S.P., Cheng, L.S., Yang, J. M., Zhang, C.Q., 2008. A review of the Cu–Ni sulphide deposits in the Chinese Tianshan and Altay orogens (Xinjiang Autonomous Region, NW China): principal characteristics and ore-forming processes. J. Asian Earth Sci. 32, 184–203.

Martin, H., 1999. Adakitic magmas: modern analogues of Archaean granitoids. Lithos 46, 411–429.

Martin, H., Moyen, J.-F., Rapp, R., 2009. The sanukitoid series: magmatism at the Archaean-Proterozoic transition. Earth Environ. Sci. Trans. R. Soc. Edin. 100, 15–33.

Martin, H., Smithies, R.H., Rapp, R., Moyen, J.F., Champion, D., 2005. An overview of adakite, tonalite–trondhjemite–granodiorite (TTG), and sanukitoid: relationships and some implications for crustal evolution. Lithos 79, 1–24.

McCarron, J.J., Smellie, J.L., 1998. Tectonic implications of fore-arc magmatism and generation of high-magnesian andesites: Alexander Island, Antarctica. J. Geol. Soc. 155, 269–280.

Middlemost, E.A., 1994. Naming materials in the magma/igneous rock system. Earth-Sci. Rev. 37, 215–224.

Miyashiro, A., 1974. Volcanic rock series in island arcs and active continental margins. Am. J. Sci. 274, 321–355.

Peccerillo, A., Taylor, S.R., 1976. Geochemistry of Eocene calc-alkaline volcanic rocks from the Kastamonu area, northern Turkey. Contrib. Miner. Petrol. 58, 63–81.

Pirajno, F., Mao, J., Zhang, Z., Zhang, Z., Chai, F., 2008. The association of mafic–ultramafic intrusions and A-type magmatism in the Tian Shan and Altay orogens, NW China: implications for geodynamic evolution and potential for the discovery of new ore deposits. J. Asian Earth Sci. 32, 165–183.

Qi, L., Grégoire, D.C., 2000. Determination of trace elements in twenty six chinese geochemistry reference materials by inductively coupled plasma-mass spectrometry. Geostandards Newsletter 24, 51–63.

Qi, L., Hu, J., Gregoire, D.C., 2000. Determination of trace elements in granites by inductively coupled plasma mass spectrometry. Talanta 51, 507–513.

Qin, K., Sun, S., Li, J., Fang, T., Wang, S., Liu, W., 2002. Paleozoic epithermal Au and porphyry Cu deposits in North Xinjiang, China: epochs, features, tectonic linkage and exploration significance. Resource Geology 52, 291–300.

Rapp, R.P., Shimizu, N., Norman, M.D., Applegate, G.S., 1999. Reaction between slab-derived melts and peridotite in the mantle wedge: experimental constraints at 3.8 GPa. Chem. Geol. 160, 335–356.

Rogers, G., Saunders, A.D., Terrell, D.J., Verma, S.P., Marriner, G.F., 1985. Geochemistry of Holocene volcanic rocks associated with ridge subduction in Baja California, Mexico. Nature 315, 389–392.
Safonova, I., Seltmann, R., Kroner, A., Gladkochub, D., Schulmann, K., Xiao, W.J., Kim, J., Komiya, T., Sun, M., 2011. A new concept of continental construction in the Central Asian Orogenic Belt (compared to actualistic examples from the Western Pacific). Episodes 34, 186–196.
Sakuyama, M., 1981. Petrological study of the Myoko and Kurohime volcanoes, Japan: crystallization sequence and evidence for magma mixing. J. Petrol. 22, 553–583.
Salters, V.J., Stracke, A., 2004. Composition of the depleted mantle. Geochem. Geophys. Geosyst. 5, Q05004.
Sengör, C.A.M., Natal'In, B.A., 1996. Turkic-type orogeny and its role in the making of the continental crust. Annu. Rev. Earth Planet. Sci. 24, 263–337.
Shimoda, G., Tatsumi, Y., Nohda, S., Ishizaka, K., Jahn, B.M., 1998. Setouchi high-Mg andesites revisited: geochemical evidence for melting of subducting sediments. Earth Planet. Sci. Lett. 160, 479–492.
Shu, L., Yu, J., Charvet, J., Laurent-Charvet, S., Sang, H., Zhang, R., 2004. Geological, geochronological and geochemical features of granulites in the Eastern Tianshan, NW China. J. Asian Earth Sci. 24, 25–41.
Shu, L.S., Deng, X.L., Zhu, W.B., Ma, D.S., Xiao, W.J., 2011. Precambrian tectonic evolution of the Tarim Block, NW China: new geochronological insights from the Quruqtagh domain. J. Asian Earth Sci. 42, 774–790.
Söderlund, U., Patchett, P.J., Vervoort, J.D., Isachsen, C.E., 2004. The ^{176}Lu decay constant determined by Lu–Hf and U–Pb isotope systematics of Precambrian mafic intrusions. Earth Planet. Sci. Lett. 219, 311–324.
Sun, S.S., McDonough, W.F., 1989. Chemical and isotopic systematics of oceanic basalts: implications for mantle composition and processes. Geol. Soc. London Spec. Publ. 42, 313–345.
Tang, G.J., Wang, Q., Wyman, D.A., Li, Z.X., Xu, Y.G., Zhao, Z.H., 2012a. Recycling oceanic crust for continental crustal growth: Sr–Nd–Hf isotope evidence from granitoids in the western Junggar region, NW China. Lithos 128, 73–83.
Tang, G.J., Wang, Q., Wyman, D.A., Li, Z.X., Zhao, Z.H., Jia, X.H., Jiang, Z.Q., 2010a. Ridge subduction and crustal growth in the Central Asian Orogenic Belt: evidence from Late Carboniferous adakites and high-Mg diorites in the western Junggar region, northern Xinjiang (west China). Chem. Geol. 277, 281–300.
Tang, G.J., Wang, Q., Wyman, D.A., Li, Z.X., Zhao, Z.H., Yang, Y.H., 2012b. Late Carboniferous high $\varepsilon Nd(t)$–$\varepsilon Hf(t)$ granitoids, enclaves and dikes in western Junggar, NW China: ridge-subduction-related magmatism and crustal growth. Lithos 140, 86–102.
Tang, G.J., Wang, Q., Wyman, D.A., Sun, M., Li, Z.X., Zhao, Z.H., Sun, W.D., Jia, X.H., Jiang, Z.Q., 2010b. Geochronology and geochemistry of Late Paleozoic magmatic rocks in the Lamasu-Dabate area, northwestern Tianshan (west China): evidence for a tectonic transition from arc to post-collisional setting. Lithos 119, 393–411.
Tang, G.J., Wyman, D.A., Wang, Q., Li, J., Li, Z.X., Zhao, Z.H., Sun, W.D., 2012c. Asthenosphere–lithosphere interaction triggered by a slab window during ridge subduction: trace element and Sr–Nd–Hf–Os isotopic evidence from Late Carboniferous tholeiites in the western Junggar area (NW China). Earth Planet. Sci. Lett. 329, 84–96.
Tatsumi, Y., 2001. Geochemical modeling of partial melting of subducting sediments and subsequent melt-mantle interaction: Generation of high-Mg andesites in the Setouchi volcanic belt, southwest Japan. Geology 29, 323–326.
Tatsumi, Y., 2006. High-Mg andesites in the Setouchi volcanic belt, southwestern Japan: analogy to Archean magmatism and continental crust formation? Annu. Rev. Earth Planet. Sci. 34, 467–499.
Tatsumi, Y., Hanyu, T., 2003. Geochemical modeling of dehydration and partial melting of subducting lithosphere: toward a comprehensive understanding of high-Mg andesite formation in the Setouchi volcanic belt, SW Japan. Geochem. Geophys. Geosyst. 4. http://dx.doi.org/10.1029/2003GC000530.
Tatsumi, Y., Ishizaka, K., 1982. Origin of high-magnesian andesites in the Setouchi volcanic belt, southwest Japan, I. petrographical and chemical characteristics. Earth Planet. Sci. Lett. 60, 293–304.
Tatsumi, Y., Shukuno, H., Sato, K., Shibata, T., Yoshikawa, M., 2003. The petrology and geochemistry of high-magnesium andesites at the western tip of the Setouchi Volcanic Belt, SW Japan. J. Petrol. 44, 1561–1578.
Taylor, R.N., Nesbitt, R.W., Vidal, P., Harmon, R.S., Auvray, B., Croudace, I.W., 1994. Mineralogy, chemistry, and genesis of the boninite series volcanics, Chichijima, Bonin Islands, Japan. J. Petrol. 35, 577–617.
Taylor, S.R., McLennan, S.M., 1985. The Continental Crust: its Composition and Evolution. Blackwell Scientific Publications, Oxford, UK, pp. 1–328.
Vervoort, J.D., Blichert-Toft, J., 1999. Evolution of the depleted mantle: Hf isotope evidence from juvenile rocks through time. Geochim. Cosmochim. Acta 63, 533–556.
Vervoort, J.D., Patchett, P.J., Gehrels, G.E., Nutman, A.P., 1996. Constraints on early Earth differentiation from hafnium and neodymium isotopes. Nature 379, 624–627.
Wang, C., Ma, R., Shu, L.S., Zhu, W.B., 1994. Study on the regional metamorphism and the tectonic settings in the eastern Tianshan orogenic belt. J. Nanjing Univ. (Nat. Sci. Ed.) 30, 494–503 (in Chinese with English abstract).
Wang, Q., Wyman, D.A., Xu, J., Dong, Y., Vasconcelos, P.M., Pearson, N., Wan, Y., Dong, H., Li, C., Yu, Y., 2008. Eocene melting of subducting continental crust and early uplifting of central Tibet: evidence from central-western Qiangtang high-K calc-alkaline andesites, dacites and rhyolites. Earth Planet. Sci. Lett. 272, 158–171.
Wang, Q., Xu, J.F., Jian, P., Bao, Z.W., Zhao, Z.H., Li, C.F., Xiong, X.L., Ma, J.L., 2006. Petrogenesis of adakitic porphyries in an extensional tectonic setting, Dexing, South China: implications for the genesis of porphyry copper mineralization. J. Petrol. 47, 119–144.
Wiedenbeck, M., Alle, P., Corfu, F., Griffin, W.L., Meier, M., Oberli, F., Quadt, A. v., Roddick, J.C., Spiegel, W., 1995. Three natural zircon standards for U–Th–Pb, Lu–Hf, trace element and REE analyses. Geostandards Newsletter 19, 1–23.
Wiedenbeck, M., Hanchar, J.M., Peck, W.H., Sylvester, P., Valley, J., Whitehouse, M., Kronz, A., Morishita, Y., Nasdala, L., Fiebig, J., 2004. Further characterisation of the 91500 zircon crystal. Geostand. Geoanal. Res. 28, 9–39.
Wilcox, R.E., Harding, T.P.t., Seely, D.R., 1973. Basic wrench tectonics. Aapg Bulletin 57, 74–96.
Windley, B.F., Alexeiev, D., Xiao, W.J., Kroner, A., Badarch, G., 2007. Tectonic models for accretion of the Central Asian Orogenic Belt. J. Geol. Soc. 164, 31–47.
Woodhead, J., Hergt, J., Shelley, M., Eggins, S., Kemp, R., 2004. Zircon Hf-isotope analysis with an excimer laser, depth profiling, ablation of complex geometries, and concomitant age estimation. Chem. Geol. 209, 121–135.
Workman, R.K., Hart, S.R., 2005. Major and trace element composition of the depleted MORB mantle (DMM). Earth Planet. Sci. Lett. 231, 53–72.
Wortel, M., Spakman, W., 2000. Subduction and slab detachment in the Mediterranean-Carpathian region. Science 290, 1910–1917.
Wu, F., Zhao, G., Wilde, S.A., Sun, D., 2005. Nd isotopic constraints on crustal formation in the North China Craton. J. Asian Earth Sci. 24, 523–545.
Wu, F.Y., Yang, Y.H., Xie, L.W., Yang, J.H., Xu, P., 2006. Hf isotopic compositions of the standard zircons and baddeleyites used in U–Pb geochronology. Chem. Geol. 234, 105–126.
Xia, L.Q., Xia, Z.C., Xu, X.Y., Li, X.M., Ma, Z.P., 2008. Relative contributions of crust and mantle to the generation of the Tianshan Carboniferous rift-related basic lavas, northwestern China. J. Asian Earth Sci. 31, 357–378.
Xiao, W., Han, C., Yuan, C., Sun, M., Lin, S., Chen, H., Li, Z., Li, J., Sun, S., 2008. Middle Cambrian to Permian subduction-related accretionary orogenesis of Northern Xinjiang, NW China: implications for the tectonic evolution of central Asia. J. Asian Earth Sci. 32, 102–117.
Xiao, W., Windley, B.F., Yong, Y., Yan, Z., Yuan, C., 2009. Early Paleozoic to Devonian multiple-accretionary model for the Qilian Shan, NW China. J. Asian Earth Sci. 35, 323–333.
Xiao, W.J., Zhang, L.C., Qin, K.Z., Sun, S., Li, J.L., 2004. Paleozoic accretionary and collisional tectonics of the eastern Tianshan (China): implications for the continental growth of central Asia. Am. J. Sci. 304, 370–395.
Xu, Y.G., Lan, J.B., Yang, Q.J., Huang, X.L., Qiu, H.N., 2008. Eocene break-off of the Neo-Tethyan slab as inferred from intraplate-type mafic dykes in the Gaoligong orogenic belt, eastern Tibet. Chem. Geol. 255, 439–453.
Yakubchuk, A., 2004. Architecture and mineral deposit settings of the Altaid orogenic collage: a revised model. J. Asian Earth Sci. 23, 761–779.
Yang, X., Tao, H., Luo, G., Ji, J., 1996. Basic features of plate tectonics in Eastern Tianshan of China. Xinjiang Geol. 14, 221–227 (in Chinese with English abstract).
Yin, J., Yuan, C., Sun, M., Long, X., Zhao, G., Wong, K.P., 2010. Late Carboniferous high-Mg dioritic dikes in Western Junggar, NW China: geochemical features, petrogenesis and tectonic implications. Gondwana Res. 17, 145–152.
Yogodzinski, G.M., Volynets, O.N., Koloskov, A.V., Seliverstov, N.I., Matvenkov, V.V., 1994. Magnesian andesites and the subduction component in a strongly calc-alkaline series at Piip Volcano, far western Aleutians. J. Petrol. 35, 163–204.
Yuan, H., Gao, S., Liu, X., Li, H., Günther, D., Wu, F., 2004. Accurate U–Pb age and trace element determinations of zircon by laser ablation-inductively coupled plasma-mass spectrometry. Geostand. Geoanal. Res. 28, 353–370.
Yuan, H.L., Gao, S., Dai, M.N., Zong, C.L., Günther, D., Fontaine, G.H., Liu, X.M., Diwu, C., 2008. Simultaneous determinations of U–Pb age, Hf isotopes and trace element compositions of zircon by excimer laser-ablation quadrupole and multiple-collector ICP-MS. Chem. Geol. 247, 100–118.
Zhang, J., Ma, C., Xiong, F., Liu, B., Li, J., Pan, Y., 2014. Early Paleozoic high-Mg diorite-granodiorite in the eastern Kunlun Orogen, western China: response to continental collision and slab break-off. Lithos 210, 129–146.
Zhang, L., Xiao, W., Qin, K., Qu, W., Du, A., 2005. Re–Os isotopic dating of molybdenite and pyrite in the Baishan Mo–Re deposit, eastern Tianshan, NW China, and its geological significance. Miner. Deposita 39, 960–969.
Zhang, L., Xiao, W., Qin, K., Zhang, Q., 2006. The adakite connection of the Tuwu-Yandong copper porphyry belt, eastern Tianshan, NW China: trace element and Sr–Nd–Pb isotope geochemistry. Miner. Deposita 41, 188–200.
Zhou, J., Ji, J., Han, B., Ma, F., Ma, Gong, J., Xu, Q., Guo, Z., 2008. ^{40}Ar/^{39}Ar Geochronology of mafic dykes in north Xinjiang. Acta Petrol. Sinica 24, 997–1010 (in Chinese with English abstract).